

# The visibility based Tapered Gridded Estimator (TGE) for the redshifted 21-cm power spectrum

Samir Choudhuri<sup>1\*</sup>, Somnath Bharadwaj<sup>1</sup>, Suman Chatterjee<sup>1</sup>, Sk. Saiyad Ali<sup>2</sup>  
 Nirupam Roy<sup>3</sup> and Abhik Ghosh<sup>4</sup>

<sup>1</sup> *Department of Physics, & Centre for Theoretical Studies, IIT Kharagpur, Pin: 721 302, India*

<sup>2</sup> *Department of Physics, Jadavpur University, Kolkata 700032, India*

<sup>3</sup> *Department of Physics, Indian Institute of Science, Bangalore 560012, India*

<sup>4</sup> *Kapteyn Astronomical Institute, PO Box 800, 9700 AV Groningen, The Netherlands*

## ABSTRACT

We present the improved visibility based Tapered Gridded Estimator (TGE) for the power spectrum of the diffuse sky signal. The visibilities are gridded to reduce the computation, and tapered through a convolution to suppress the contribution from the outer regions of the telescope’s field of view. The TGE also internally estimates the noise bias, and subtracts this out to give an unbiased estimate of the power spectrum. An earlier version of the 2D TGE for the angular power spectrum  $C_\ell$  is improved and then extended to obtain the 3D TGE for the power spectrum  $P(\mathbf{k})$  of the 21-cm brightness temperature fluctuations. Analytic formulas are also presented for predicting the variance of the binned power spectrum. The estimator and its variance predictions are validated using simulations of 150 MHz GMRT observations. We find that the estimator accurately recovers the input model for the 1D Spherical Power Spectrum  $P(k)$  and the 2D Cylindrical Power Spectrum  $P(k_\perp, k_\parallel)$ , and the predicted variance is also in reasonably good agreement with the simulations.

**Key words:** methods: statistical, data analysis - techniques: interferometric- cosmology: diffuse radiation

## 1 INTRODUCTION

Observations of the redshifted neutral hydrogen (HI) 21-cm radiation hold the potential of probing a wide range of cosmological and astrophysical phenomena over a large redshift range  $0 < z \lesssim 200$  (Bharadwaj & Ali 2005; Furlanetto, Oh & Briggs. 2006; Morales & Wyithe 2010; Prichard & Loeb 2012; Mellema et al. 2013). There now are several ongoing experiments such as the Donald C. Backer Precision Array to Probe the Epoch of Reionization (PAPER<sup>1</sup>, Parsons et al. 2010), the Low Frequency Array (LOFAR<sup>2</sup>, van Haarlem et al. 2013; Yatawatta et al. 2013) and the Murchison Wide-field Array (MWA<sup>3</sup> Bowman et al. 2013; Tingay et al. 2013) which aim to measure the power spectrum of the 21-cm radiation from the Epoch of Reionization (EoR,  $6 \lesssim z \lesssim 13$ ). Future telescopes like the Square Kilometer Array (SKA1 LOW<sup>4</sup>, Koopmans et al. 2015) and the Hydrogen Epoch of Reionization Array (HERA<sup>5</sup>, Neben et al. 2016) are planned to achieve even higher sensitivity for measuring the EoR 21-cm power spectrum. Several other upcoming experiments like the Ooty Wide Field Array (OWFA; Prasad & Subrahmanya 2011; Ali & Bharadwaj 2014), the Canadian Hydrogen Intensity Mapping Experiment (CHIME<sup>6</sup>; Bandura et al. 2014), the Baryon Acoustic Oscillation Broadband, Broad Beam Array (BAOBAB<sup>7</sup>; Pober et al. 2013a) and the Square Kilometre Array (SKA1 MID; Bull et al. 2015) target the post-Reionization 21-cm signal ( $0 < z \lesssim 6$ ).

\* Email:samir11@phy.iitkgp.ernet.in

<sup>1</sup> <http://astro.berkeley.edu/dbacker/eor>

<sup>2</sup> <http://www.lofar.org/>

<sup>3</sup> <http://www.mwatelescope.org>

<sup>4</sup> <http://www.skatelescope.org/>

<sup>5</sup> <http://reionization.org/>

<sup>6</sup> <http://chime.phas.ubc.ca/>

<sup>7</sup> <http://bao.berkeley.edu/>

Despite the sensitive new instruments, the main challenge still arises from the fact that the cosmological 21-cm signal is buried in astrophysical foregrounds which are 4 – 5 orders of magnitude brighter (Shaver et al. 1999; Di Matteo et al. 2002; Santos et al. 2005; Ali, Bharadwaj & Chengalur 2008; Paciga et al. 2011; Ghosh et al. 2011a,b). A large variety of techniques have been proposed to overcome this problem and estimate the 21-cm power spectrum. The different approaches may be broadly divided into two classes (1.) Foreground Removal, and (2.) Foreground Avoidance.

The idea in Foreground Removal is to model the foregrounds and subtract these out either directly from the data (eg. Ali, Bharadwaj & Chengalur 2008) or from the power spectrum estimator after correlating the data (eg. Ghosh et al. 2011a,b). Foreground Removal is a topic of intense current research (Jelić et al. 2008; Bowman et al. 2009; Paciga et al. 2011; Chapman et al. 2012; Parsons et al. 2012; Liu & Tegmark 2012; Trott et al. 2012; Pober et al. 2013; Paciga et al. 2013; Parsons et al. 2014; Trott et al. 2016).

Various studies (eg. Datta et al. 2010) show that the foreground contribution to the Cylindrical Power Spectrum  $P(k_{\perp}, k_{\parallel})$  is expected to be restricted within a wedge in the two dimensional (2D)  $(k_{\perp}, k_{\parallel})$  plane. The idea in Foreground Avoidance is to avoid the Fourier modes within the foreground wedge and only use the uncontaminated modes outside the wedge to estimate the 21-cm power spectrum (Vedantham et al. 2012; Thyagarajan et al. 2013; Pober et al. 2014; Liu et al. 2014a,b; Dillon et al. 2014, 2015; Ali et al. 2015). In a recent paper Jacobs et al. (2016) have compared several power spectrum estimation techniques in the context of MWA.

Point sources dominate the low frequency sky at the angular scales  $\leq 4^{\circ}$  (Ali, Bharadwaj & Chengalur 2008) which are relevant for EoR 21-cm power spectrum with the telescopes like the GMRT, LOFAR and the upcoming SKA. It is difficult to model and subtract the point sources which are located at the periphery of the telescope’s field of view (FoV). The antenna response deviates from circular symmetry, and is highly frequency and time dependent at the outer parts of the telescope’s FoV. The calibration also differs from the phase center due to ionospheric fluctuations. The residual point sources located far away from the phase centre cause the signal to oscillates along the frequency direction (Ghosh et al. 2011a,b). This poses a severe problem for foreground removal techniques which assume a smooth behavior of the signal along the frequency direction. Equivalently, these distant point sources reduce the EoR window by increasing the area under the foreground wedge in  $(k_{\perp}, k_{\parallel})$  space (Thyagarajan et al. 2015). In a recent paper, Pober et al. (2016) showed that correctly modelling and subtracting the distant point sources are important for detecting the redshifted 21-cm signal. Point source subtraction is also important for measuring the angular power spectrum of the diffuse Galactic synchrotron radiation (Bernardi et al. 2009; Ghosh et al. 2012; Iacobelli et al. 2013). Apart from being an important foreground component for the EoR 21-cm signal, this is also interesting in its own right.

It is possible to suppress the contribution from the outer parts of the telescope’s FoV by tapering the sky response through a suitably chosen window function. Ghosh et al. (2011b) have analyzed 610MHz GMRT data to show that it is possible to implement the tapering by convolving the observed visibilities with the Fourier transform of the window function. It is found that this reduces the amplitude of the oscillation along the frequency direction. Our earlier work Choudhuri et al. (2014) (hereafter Paper I) has introduced the Tapered Gridded Estimator (TGE) which places the findings of Ghosh et al. (2011b) on a sound theoretical footing. Considering observations at a single frequency, the TGE estimates the angular power spectrum  $C_{\ell}$  of the 2D sky signal directly from the measured visibilities while simultaneously tapering the sky response. As a test-bed for the TGE, Paper I considers a situation where the point sources have been identified and subtracted out so that the residual visibilities are dominated by the Galactic synchrotron radiation. This has been used to investigate how well the TGE is able to recover the angular power spectrum of the input model used to simulate the Galactic synchrotron emission at 150 MHz. While most of the analysis was for the GMRT, simulations for LOFAR were also considered. These investigations show that the TGE is able to recover the input model  $C_{\ell}^M$  to a high level of precision provided the baselines have a uniform  $uv$  coverage. For the GMRT, which has a patchy  $uv$  coverage, the  $C_{\ell}$  is somewhat overestimated using TGE though the excess is largely within the  $1\sigma$  errors. This deviation is found to be reduced in a situation with a more uniform and denser baseline distribution, like LOFAR. Paper I also analyzes the effects of gain errors and the  $w$ -term.

In a recent paper Choudhuri et al. (2016) (hereafter Paper II) we have further developed the simulations of Paper I to include the point sources. We have used conventional radio astronomical techniques to model and subtract the point sources from the central region of the primary beam. As detailed in Paper II, it is difficult to do the same for the sources which are far away from the phase center, and these persist as residuals in the visibility data. We find that these residual point sources dominate the  $C_{\ell}$  estimated at large baselines. We also show that it is possible to suppress the contribution from these residual sources located at the periphery of the FoV by using TGE with a suitably chosen window function.

Removing the noise bias is an important issue for any power spectrum estimator. As demonstrated in Paper II, the TGE internally estimates the actual noise bias from the data and subtracts this out to give an unbiased estimate of the power spectrum.

In the present work we report the progress on two counts. First, our earlier implementation of the TGE assumed a uniform and dense baseline  $uv$  coverage to calculate the normalization coefficient which relates visibility correlations to the estimated angular power spectrum  $C_{\ell}$ . We, however, found (Paper I) that this leads to an overestimate of  $C_{\ell}$  for instruments like the GMRT which have a sparse and patchy  $uv$  coverage. In Section 2 of this paper we present an improved TGE which

overcomes this problem by using simulations to estimate the normalization coefficient. Second, the entire analysis of Papers I and II has been restricted to observations at a single frequency wherein the relevant issue is to quantify the 2D angular fluctuations of the sky signal. This, however, is inadequate for the three dimensional (3D) redshifted HI 21-cm signal where it is necessary to also simultaneously quantify the fluctuations along the frequency direction. In Section 3 of this paper we have generalized the TGE to quantify the 3D 21-cm signal and estimate the spatial power spectrum of the 21-cm brightness temperature fluctuations  $P(\mathbf{k})$ . We discuss two different binning schemes which respectively yield the spherically-averaged (1D) power spectrum  $P(k)$  and the cylindrically-averaged (2D) power spectrum  $P(k_\perp, k_\parallel)$ , and present theoretical expressions for predicting the expected variance. We have validated the estimator and its variance predictions using simulations which are described in Section 4 and for which the results are presented in Section 5. Sections 6 presents the summary and conclusions.

In this paper, we have used cosmological parameters from the (Planck + WMAP) best-fit  $\Lambda$ CDM cosmology (Planck Collaboration, P. A. R. Ade et al. 2015).

## 2 $C_\ell$ ESTIMATION

### 2.1 An Improved TGE

In this section we restrict our attention to a single frequency channel  $\nu_a$  which we do not show explicitly in any of the subsequent equations. The measured visibilities  $\mathcal{V}_i$  can be decomposed into two contributions,

$$\mathcal{V}_i = \mathcal{S}(\mathbf{U}_i) + \mathcal{N}_i \quad (1)$$

the sky signal and system noise respectively, and  $\mathbf{U}_i$  is the baseline corresponding to the  $i$ -th visibility. The signal contribution  $\mathcal{S}(\mathbf{U}_i)$  records the Fourier transform of the product of the telescope's primary beam pattern  $\mathcal{A}(\theta)$  and the specific intensity fluctuation on the sky  $\delta I(\theta)$ . Expressing the signal in terms of brightness temperature fluctuations  $\delta T(\theta)$  we have

$$\mathcal{S}(\mathbf{U}_i) = \left( \frac{\partial B}{\partial T} \right) \int d^2\theta e^{2\pi i \mathbf{U}_i \cdot \theta} \mathcal{A}(\theta) \delta T(\theta), \quad (2)$$

where  $B = 2k_B T / \lambda^2$  is the Planck function in the Raleigh-Jeans limit which is valid at the frequencies of our interest. In terms of Fourier components we have

$$\mathcal{S}(\mathbf{U}_i) = \left( \frac{\partial B}{\partial T} \right) \int d^2U \tilde{a}(\mathbf{U}_i - \mathbf{U}) \Delta \tilde{T}(\mathbf{U}), \quad (3)$$

where  $\Delta \tilde{T}(\mathbf{U})$  and  $\tilde{a}(\mathbf{U})$  are the Fourier transforms of  $\delta T(\theta)$  and  $\mathcal{A}(\theta)$  respectively. Here we assume that  $\delta T(\theta)$  is a particular realization of a statistically homogeneous and isotropic Gaussian random process on the sky. Its statistical properties are completely characterized by the angular power spectrum of the brightness temperature fluctuations  $C_\ell$  defined through

$$\langle \Delta \tilde{T}(\mathbf{U}) \Delta \tilde{T}^*(\mathbf{U}') \rangle = \delta_D^2(\mathbf{U} - \mathbf{U}') C_{2\pi U} \quad (4)$$

where  $\delta_D^2(\mathbf{U} - \mathbf{U}')$  is a two dimensional Dirac delta function and  $2\pi U = \ell$ , is the angular multipole. The angular brackets  $\langle \dots \rangle$  here denote an ensemble average over different realizations of the stochastic temperature fluctuations on the sky.

The noise in the different visibilities is uncorrelated, and we have

$$\langle \mathcal{V}_i \mathcal{V}_j \rangle = \langle \mathcal{S}_i \mathcal{S}_j \rangle + \langle |\mathcal{N}_i|^2 \rangle \delta_{i,j} \quad (5)$$

where  $\langle |\mathcal{N}_i|^2 \rangle$  is the noise variance of the visibilities,  $\delta_{i,j}$  is a Kronecker delta and

$$\langle \mathcal{S}_i \mathcal{S}_j \rangle = \left( \frac{\partial B}{\partial T} \right)^2 \int d^2U \tilde{a}(\mathbf{U}_i - \mathbf{U}) \tilde{a}^*(\mathbf{U}_j - \mathbf{U}) C_{2\pi U_i} \quad (6)$$

This convolution can be approximated by a multiplying factor if  $C_{2\pi U}$  is nearly constant across the width of  $\tilde{a}(\mathbf{U}_i - \mathbf{U})$ , which is the situation at large baselines where the antenna separation is large compared to the telescope diameter (Paper I), and we have

$$\langle |\mathcal{V}_i|^2 \rangle = V_0 C_{2\pi U_i} + \langle |\mathcal{N}_i|^2 \rangle \quad (7)$$

where

$$V_0 = \left( \frac{\partial B}{\partial T} \right)^2 \int d^2U |\tilde{a}(\mathbf{U}_i - \mathbf{U})|^2. \quad (8)$$

We see that the correlation of a visibility with itself provides an estimate of the angular power spectrum, except for the terms  $\langle |\mathcal{N}_i|^2 \rangle$  which introduce a positive noise bias.

It is possible to control the sidelobe response of the telescope's beam patten  $\mathcal{A}(\theta)$  by tapering the sky response through a frequency independent window function  $\mathcal{W}(\theta)$ . In this work we use a Gaussian  $\mathcal{W}(\theta) = e^{-\theta^2/\theta_w^2}$  with  $\theta_w$  chosen so that the window function cuts off the sky response well before the first null of  $\mathcal{A}(\theta)$ . This tapering is achieved by convolving the

measured visibilities with the Fourier transform of  $\mathcal{W}(\theta)$ . We choose a rectangular grid in the  $uv$  plane and consider the convolved visibilities

$$\mathcal{V}_{cg} = \sum_i \tilde{w}(\mathbf{U}_g - \mathbf{U}_i) \mathcal{V}_i \quad (9)$$

where  $\tilde{w}(\mathbf{U}) = \pi\theta_w^2 e^{-\pi^2 U^2 \theta_w^2}$  is the Fourier transform of  $\mathcal{W}(\theta)$  and  $\mathbf{U}_g$  refers to the different grid points. As shown in Paper I, gridding reduces the computation in comparison to an estimator that uses pairs of visibilities to estimate the power spectrum. We now focus our attention on  $\mathcal{S}_{cg}$  which is the sky signal contribution to  $\mathcal{V}_{cg}$ . This can be written as

$$\mathcal{S}_{cg} = \left( \frac{\partial B}{\partial T} \right) \int d^2 U \tilde{K}(\mathbf{U}_g - \mathbf{U}) \Delta \tilde{T}(\mathbf{U}), \quad (10)$$

where

$$\tilde{K}(\mathbf{U}_g - \mathbf{U}) = \int d^2 U' \tilde{w}(\mathbf{U}_g - \mathbf{U}') B(\mathbf{U}') \tilde{a}(\mathbf{U}' - \mathbf{U}) \quad (11)$$

is an effective ‘‘gridding kernel’’, and

$$B(\mathbf{U}) = \sum_i \delta_D^2(\mathbf{U} - \mathbf{U}_i) \quad (12)$$

is the baseline sampling function of the measured visibilities.

Proceeding in exactly the same way as we did for eq. (7) we have

$$\langle |\mathcal{V}_{cg}|^2 \rangle = V_{1g} C_{2\pi U_g} + \sum_i |\tilde{w}(\mathbf{U}_g - \mathbf{U}_i)|^2 \langle |\mathcal{N}_i|^2 \rangle, \quad (13)$$

where

$$V_{1g} = \left( \frac{\partial B}{\partial T} \right)^2 \int d^2 U |\tilde{K}(\mathbf{U}_g - \mathbf{U})|^2. \quad (14)$$

Here again we see that the correlation of the tapered gridded visibility with itself provides an estimate of the angular power spectrum, except for the terms  $\langle |\mathcal{N}_i|^2 \rangle$  which introduces a positive noise bias.

Combining equations (7) and (13) we have

$$\left\langle \left( |\mathcal{V}_{cg}|^2 - \sum_i |\tilde{w}(\mathbf{U}_g - \mathbf{U}_i)|^2 |\mathcal{V}_i|^2 \right) \right\rangle = M_g C_{2\pi U_g} \quad (15)$$

where

$$M_g = V_{1g} - \sum_i |\tilde{w}(\mathbf{U}_g - \mathbf{U}_i)|^2 V_0 \quad (16)$$

This allows us to define the Tapered Gridded Estimator (TGE) as

$$\hat{E}_g = M_g^{-1} \left( |\mathcal{V}_{cg}|^2 - \sum_i |\tilde{w}(\mathbf{U}_g - \mathbf{U}_i)|^2 |\mathcal{V}_i|^2 \right). \quad (17)$$

The TGE defined here (eq. 17) incorporates three novel features which are highlighted below. First, the estimator uses the gridded visibilities to estimate  $C_{\ell}$ , this is computationally much faster than individually correlating the visibilities. Second, the correlation of the gridded visibilities is used to estimate  $C_{\ell}$ . A positive noise bias is removed by subtracting the auto-correlation of the visibilities. Third, the estimator allows us to taper the FoV so as to restrict the contribution from the sources in the outer regions and the sidelobes. It is, however, necessary to note that this comes at a cost which we now discuss. First, we lose information at the largest angular scales due to the reduced FoV. This restricts the smallest  $\ell$  value at which it is possible to estimate the power spectrum. Second, the reduced FoV results in a larger cosmic variance for the smaller angular modes which are within the tapered FoV.

The TGE provides an unbiased estimate of  $C_{\ell_g}$  at the angular multipole  $\ell_g = 2\pi U_g$  *i.e.*

$$\langle \hat{E}_g \rangle = C_{\ell_g} \quad (18)$$

We use this to define the binned Tapered Gridded Estimator for bin  $a$

$$\hat{E}_G(a) = \frac{\sum_g w_g \hat{E}_g}{\sum_g w_g}. \quad (19)$$

where  $w_g$  refers to the weight assigned to the contribution from any particular grid point. In the entire subsequent analysis we have used the weight  $w_g = 1$  which assigns equal weightage to all the grid points which are sampled by the baselines.

The binned estimator has an expectation value

$$\bar{C}_{\bar{\ell}_a} = \frac{\sum_g w_g C_{\ell_g}}{\sum_g w_g} \quad (20)$$

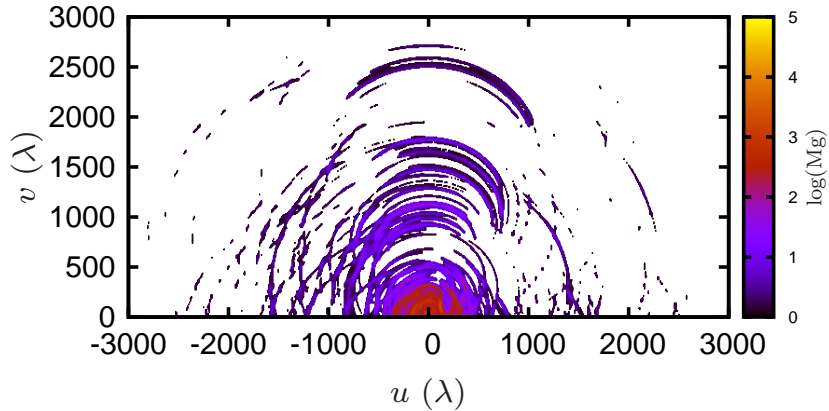


**Figure 1.** This shows  $M_g$  for a fixed value of  $f = 0.6$ . Note that, the baselines in the lower half of the  $uv$  plane have been folded on to the upper half.

where  $\bar{C}_{\bar{\ell}_a}$  is the average angular power spectrum at

$$\bar{\ell}_a = \frac{\sum_g w_g \ell_g}{\sum_g w_g} \quad (21)$$

which is the effective angular multipole for bin  $a$ .

## 2.2 Calculating $M_g$

The discussion, till now, has not addressed how to calculate  $M_g$  which is the normalization constant for the TGE (eq. 17). The values of  $M_g$  (eq. 16) depend on the baseline distribution (eq. 12) and the form of the tapering function  $\mathcal{W}(\theta)$ , and it is necessary to calculate  $M_g$  at every grid point in the  $uv$  plane. Our earlier work (Paper I) presents an analytic approximation using which it is possible to estimate  $M_g$ . While this has been found to work very well in a situation where the baselines have a nearly uniform and dense  $uv$  coverage (Fig. 7 of Paper I), it leads to an overestimate of  $C_\ell$  if we have a sparse and non-uniform  $uv$  coverage. Here we present a different method to estimate  $M_g$  which, as we show later, works very well even if we have a sparse and non-uniform  $uv$  coverage.

We proceed by calculating simulated visibilities  $[\mathcal{V}_i]_{\text{UPAS}}$  corresponding to an unit angular power spectrum (UAPS) which has  $C_\ell = 1$  with exactly the same baseline distribution as the actual observed visibilities. We then have (eq. 15)

$$M_g = \left\langle \left( |\mathcal{V}_{cg}|^2 - \sum_i |\tilde{w}(\mathbf{U}_g - \mathbf{U}_i)|^2 \langle |\mathcal{V}_i|^2 \rangle \right)_{\text{UPAS}} \right\rangle \quad (22)$$

which allows us to estimate  $M_g$ . We average over  $N_u$  independent realizations of the UPAS to reduce the statistical uncertainty ( $\delta M_g / M_g \sim 1/\sqrt{N_u}$ ) in the estimated  $M_g$ .

## 2.3 Validating the estimator

We have tested the entire method of analysis using simulations of 8 hours of 150 MHz GMRT observations targeted on an arbitrarily selected field located at RA=10h46m00s and DEC=59° 00' 59". The simulations only incorporate the diffuse Galactic synchrotron radiation for which we use the measured angular power spectrum (Ghosh et al. 2012)

$$C_\ell^M = A_{150} \times \left( \frac{1000}{\ell} \right)^\beta \quad (23)$$

as the input model to generate the brightness temperature fluctuations on the sky. Here  $A_{150} = 513 \text{ mK}^2$  and  $\beta = 2.34$  (Ghosh et al. 2012). The simulation covers a  $\sim 26.4^\circ \times 26.4^\circ$  region of the sky, which is slightly more than ten times the FWHM of the GMRT primary beam ( $\theta_{\text{FWHM}} = 157'$ ). The diffuse signal was simulated on a grid of resolution  $\sim 0.5'$ , and the entire

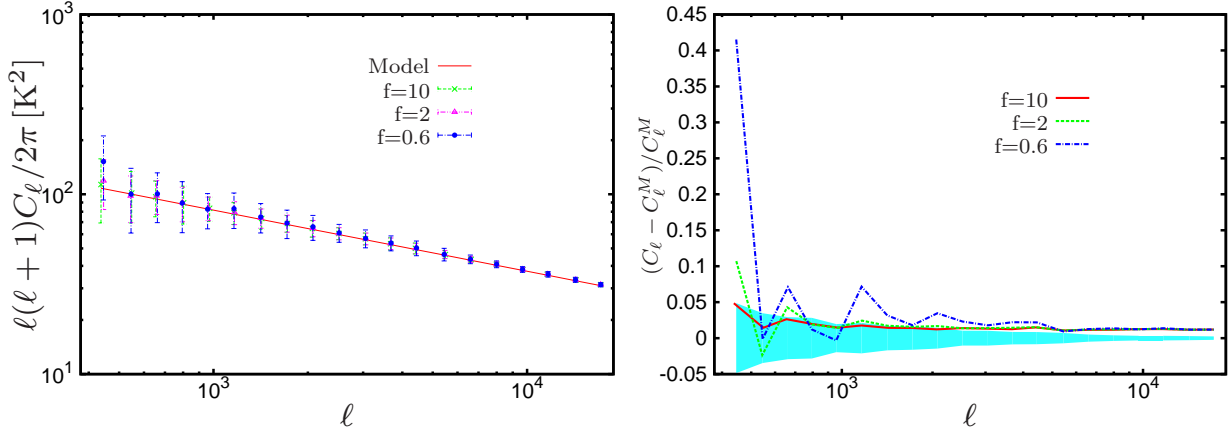


**Figure 2.** The left panel shows a comparison of the input model and the values recovered from the simulated visibilities using the improved TGE for different tapering of values  $f = 10, 2$  and  $0.6$ , with  $1\text{-}\sigma$  error bars estimated from  $N_r = 128$  realizations of the simulations. The right panel shows the fractional deviation of the estimated  $C_\ell$  with respect to the input model. Here the shaded region shows the expected statistical fluctuations ( $\sigma_{EG}/\sqrt{N_r}C_\ell^M$ ) of the fractional deviation for  $f = 0.6$ .

analysis was restricted to baselines within  $U \leq 3,000$ . Our earlier work (Paper II), and also the discussion of this paper, show that the noise bias cancels out from the TGE, and we have not included the system noise in these simulations.

We have modelled the tapering window function as a Gaussian  $\mathcal{W}(\theta) = e^{-\theta^2/\theta_w^2}$  where we parametrize  $\theta_w = f\theta_0$  where  $\theta_0 = 0.6 \times \theta_{FWHM}$ , and preferably  $f \leq 1$  so that  $\mathcal{W}(\theta)$  cuts off the sky response well before the first null of the primary beam. After tapering, we have an effective beam pattern  $\mathcal{A}_W(\theta) = \mathcal{W}(\theta)\mathcal{A}(\theta, \nu)$  which is well approximated by a Gaussian  $\mathcal{A}_W(\theta) = e^{-\theta^2/\theta_1^2}$  with  $\theta_1 = f(1+f^2)^{-1/2}\theta_0$ . The spacing of the  $uv$  grid required for TGE is decided by  $\tilde{a}_W(U) = \pi\theta_1^2 e^{-\pi^2 U^2 \theta_1^2}$  which is the Fourier transform of  $\mathcal{A}_W(\theta)$ . We have chosen a grid spacing  $\Delta U = \sqrt{\ln 2}/(2\pi\theta_1)$  which corresponds to one fourth of the FWHM of  $\tilde{a}_W(U)$ . The convolution in eq. (9) was restricted to the visibilities within a disc of radius  $12 \times \Delta U$  around each grid point. The function  $\tilde{w}(\mathbf{U}_g - \mathbf{U}_i)$  falls off rapidly and we do not expect the visibilities beyond this to make a significant contribution.

We have considered three different values  $f = 10, 2$  and  $0.6$  for the tapering, here  $f = 10$  essentially corresponds to a situation with no tapering, and the sky response gets confined to a progressively smaller region as the value of  $f$  is reduced to  $f = 2.0$  and  $0.6$  respectively (see Figure 1 of Paper II). We have used  $N_u = 128$  independent realizations of the UAPS to estimate  $M_g$  for each point in the  $uv$  grid. It is necessary to separately calculate  $M_g$  for each value of  $f$ . Figure 1 shows the values of  $M_g$  for  $f = 0.6$ . We see that this roughly traces out the  $uv$  tracks of the baselines, the convolution with  $\tilde{w}(\mathbf{U}_g - \mathbf{U}_i)$  results in a thickening of the tracks. The values of  $M_g$  are roughly proportional to  $N_g^2 - N_g$ , where  $N_g$  is the number of visibilities that contribute to any particular grid point.

The estimator (eq. 17) was applied to the simulated visibility data which was generated using the model angular power spectrum (eq. 23). The estimated angular power spectrum was binned into 20 annular bins of equal logarithmic spacing. We have used  $N_r = 128$  independent realizations of the simulation to calculate the mean and standard deviation of  $C_\ell$  shown in the left panel of Figure 2. We see that the TGE is able to recover the input model  $C_\ell^M$  quite accurately. As mentioned earlier, our previous implementation of TGE (Paper I) had a problem in that the estimated  $C_\ell$  was in all cases in excess of the input model  $C_\ell^M$ , though the deviations were within the  $1\sigma$  error bars throughout. The right panel of Figure 2 shows the fractional deviation  $(C_\ell - C_\ell^M)/C_\ell^M$  for the improved TGE introduced in this paper for the three different values of  $f$  mentioned earlier. We see that for all the values of  $f$  the fractional deviation is less than 10% for  $\ell \geq 500$ . This is a considerable improvement over the results of Paper I where we had 20% to 50% deviations. The fractional deviation is seen to increase as we increase the tapering *i.e.* reduce the value of  $f$ . We see that for  $f = 10$  and  $2$ , the fractional deviation is less than 3% for all values of  $\ell$  except at the smallest bin. The fractional deviation for  $f = 0.6$  is less than 5% except at the smallest value of  $\ell$  where it becomes almost 40%. This is possibly an outcome of the fact that the width of the convolution window  $\tilde{w}(\mathbf{U}_g - \mathbf{U}_i)$  increases as the value of  $f$  is reduced, and the variation of the signal amplitude within the width of  $\tilde{w}(\mathbf{U}_g - \mathbf{U}_i)$  becomes important at small baselines where it is reflected as an overestimate of the value of  $C_\ell$ . Theoretically, we expect the fractional deviation to have random, statistical fluctuations of the order  $\sigma_{EG}/\sqrt{N_r}C_\ell^M$ , where  $\sigma_{EG}$  is the standard deviation of the estimated angular power spectrum. We have shown the statistical fluctuation expected for  $f = 0.6$  as a shaded region in the right panel of Figure 2. We see that the fractional deviation is roughly consistent with statistical fluctuations for  $\ell \geq 500$ .



## 2.4 Variance

In the preceding discussion we have used several statistically independent realizations of the signal to determine the variance of the estimated binned angular power spectrum. Such a procedure is, by and large, only possible with simulated data. We usually have access to only one statistically independent realization of the input signal, and the aim is to use this to not only estimate the angular power spectrum but also estimate the uncertainty in the estimated angular power spectrum. In this subsection we present theoretical predictions for the variance of the binned TGE (eq. (19))

$$\sigma_{E_G}^2(a) = \langle \hat{E}_G^2(a) \rangle - \langle \hat{E}_G(a) \rangle^2 \quad (24)$$

which can be used to estimate the uncertainty in the measured angular power spectrum. Following Paper I, we ignore the term  $\sum_i |\tilde{w}(\mathbf{U}_g - \mathbf{U}_i)|^2 |\mathcal{V}_i|^2$  in eq. (17) for calculating the variance. The signal contribution from this term to the estimator at the grid point  $\mathbf{U}_g$  scales as  $N_g$  which is the number of visibilities that contribute to  $\hat{E}_g$ . In comparison to this, the contribution from the term  $|\mathcal{V}_{cg}|^2$  scales as  $N_g^2$  which is much larger when  $N_g \gg 1$ . Assuming that this condition is satisfied at every grid point which contributes to the binned TGE, it is justified to drop the term  $\sum_i |\tilde{w}(\mathbf{U}_g - \mathbf{U}_i)|^2 |\mathcal{V}_i|^2$  for calculating the variance. We then have

$$\sigma_{E_G}^2(a) = \frac{\sum_{gg'} w_g w_{g'} M_g^{-1} M_{g'}^{-1} |\langle \mathcal{V}_{cg} \mathcal{V}_{cg'}^* \rangle|^2}{[\sum_g w_g]^2} \quad (25)$$

which is identical to eq. (41) of Paper I, except that we now have the normalization constant  $M_g^{-1}$  instead of  $K_{1g}^{-2}/V_1$ .

It is necessary to model the correlation between the convolved visibilities at two different grid points  $\langle \mathcal{V}_{cg} \mathcal{V}_{cg'}^* \rangle$  in eq. (25) in order to make further progress. This correlation is a sum of two parts

$$\langle \mathcal{V}_{cg} \mathcal{V}_{cg'}^* \rangle = \langle \mathcal{S}_{cg} \mathcal{S}_{cg'}^* \rangle + \langle \mathcal{N}_{cg} \mathcal{N}_{cg'}^* \rangle \quad (26)$$

the signal and the noise correlation respectively.

Earlier studies (Paper I) show that we expect the signal correlation  $\langle \mathcal{S}_{cg} \mathcal{S}_{cg'}^* \rangle$  to fall off as  $e^{-|\Delta \mathbf{U}_{gg'}|^2 / \sigma_1^2}$  if the grid separation is increased, here  $\sigma_1 = f^{-1} \sqrt{1 + f^2} \sigma_0$  where  $\sigma_0 = 0.76 / \theta_{\text{FWHM}}$ . We use this to approximate the signal correlation as

$$\langle \mathcal{S}_{cg} \mathcal{S}_{cg'}^* \rangle = \sqrt{M_g M_{g'}} e^{-|\Delta \mathbf{U}_{gg'}|^2 / \sigma_1^2} \bar{C}_{\bar{\ell}_a} \quad (27)$$

where  $\bar{C}_{\bar{\ell}_a}$  refers to the angular power spectrum measured at the particular bin  $a$  for which the variance  $\sigma_{E_G}^2(a)$  is being calculated.

The noise correlation

$$\langle \mathcal{N}_{cg} \mathcal{N}_{cg'}^* \rangle = \sum_i \tilde{w}(\mathbf{U}_g - \mathbf{U}_i) \tilde{w}^*(\mathbf{U}_{g'} - \mathbf{U}_i) \langle |\mathcal{N}_i|^2 \rangle \quad (28)$$

also is expected to fall off as the grid separation is increased, and we have modeled this  $|\Delta \mathbf{U}_{gg'}|$  dependence as

$$\langle \mathcal{N}_{cg} \mathcal{N}_{cg'}^* \rangle = \sqrt{K_{2gg} K_{2g'g'}} e^{-|\Delta \mathbf{U}_{gg'}|^2 / \sigma_n^2} (2\sigma_n^2) \quad (29)$$

where,  $K_{2gg} = \sum_i |\tilde{w}(\mathbf{U}_g - \mathbf{U}_i)|^2$ ,  $\sigma_n = 3\sigma_0 f^{-1}$  and  $\sigma_n^2$  is the variance of the real (and also imaginary) part of  $\mathcal{N}_i$ .

We have used eqs. (29), (27) and (26) in eq. (25) to calculate  $\sigma_{E_G}^2(a)$ , the analytic prediction for the variance of the estimated binned angular power spectrum  $\bar{C}_{\bar{\ell}_a}$ .

The left panel of Figure 3 shows the analytic prediction for the variance calculated using eq. (25) for a fixed value of  $f = 0.6$ . For comparison we also show the variance estimated from  $N_r = 128$  independent realizations of the simulated visibilities. We have considered two situations, the first where the simulated visibilities only have the signal corresponding to the input model (eq. 23) and no system noise, and the second situation where in addition to the signal the visibilities also have a system noise contribution with  $\sigma_n = 1.03$  Jy which corresponds to 16 s integration time and a channel width of 125 kHz. We see that the variance calculated from the simulations is dominated by cosmic variance at small  $\ell$  ( $\leq 2,000$ ) where the variance does not change irrespective of whether we include the system noise or not. The variance calculated from the simulations is dominated by the system noise at large  $\ell$  ( $\geq 5,000$ ). We see that the analytic predictions are in reasonably good agreement with the values obtained from the simulations over the entire  $\ell$  range that we have considered here. We have also considered situations where  $f = 2.0$  and 10 for which the comparison with the analytic results are not shown here. In all cases we find that analytic predictions are in reasonably good agreement with the values obtained from the simulations.

The right panel of Figure 3 shows how the variance obtained from the simulations changes with  $f$ . We see that at low  $\ell$  the variance increases if the value of  $f$  is reduced. This is a consequence of the fact that cosmic variance increases as the sky response is tapered by reducing  $f$ . The same effect has also been discussed in detail in our earlier paper (Paper I). We also see that at large  $\ell$  the variance is considerably higher for  $f = 10$  in comparison with  $f = 2$  and 0.6. This  $\ell$  range is dominated by the system noise contribution. The number of independent visibilities which are combined to estimate the power spectrum at any grid point increases as  $f$  is reduced, and this is reflected in a smaller variance as  $f$  is reduced.

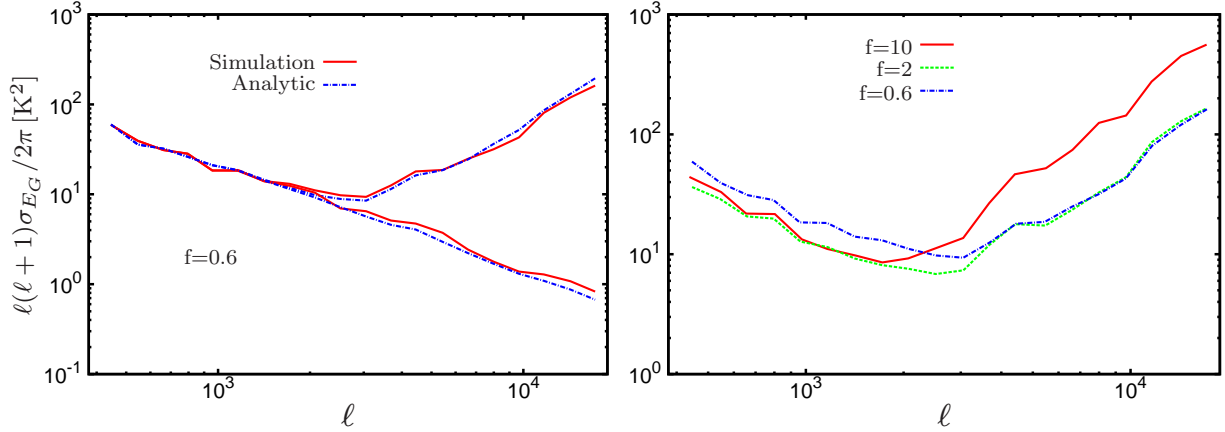


**Figure 3.** In the left panel the analytic prediction for the variance (eq. 25) is compared with variance estimated from  $N_r = 128$  realizations of the simulated visibilities. Results are shown both with (upper curves) and without (lower curves) the system noise contribution. Both match at small  $\ell$  where cosmic variance dominates, the system noise however is important at large  $\ell$  where the two sets of results are different. The right panel shows how the variance with system noise obtained from simulations varies for different values of  $f$ .

### 3 3D $P(\mathbf{k}_\perp, k_\parallel)$ ESTIMATION

#### 3.1 3D TGE

We now turn our attention to the redshifted 21-cm HI brightness temperature fluctuations where it is necessary to consider different frequency channels for which eq. (1) is generalized to

$$\mathcal{V}_i(\nu_a) = \mathcal{S}(\mathbf{U}_i, \nu_a) + \mathcal{N}_i(\nu_a). \quad (30)$$

Proceeding in exactly the same manner as for a single frequency channel (eq. 2), we have

$$\mathcal{S}(\mathbf{U}_i, \nu_a) = \left( \frac{\partial B}{\partial T} \right)_{\nu_a} \int d^2\theta e^{2\pi i \mathbf{U}_i \cdot \theta} \mathcal{A}(\theta, \nu_a) \delta T(\theta, \nu_a), \quad (31)$$

and the noise in the different visibility measurements at different frequency channels are uncorrelated

$$\langle \mathcal{N}_i(\nu_a) \mathcal{N}_j(\nu_b) \rangle = \langle |\mathcal{N}_i(\nu_a)|^2 \rangle \delta_{i,j} \delta_{a,b}. \quad (32)$$

Note that the baseline corresponding to a fixed antenna separation  $\mathbf{U}_i = \mathbf{d}_i/\lambda$ , the antenna beam pattern  $\mathcal{A}(\theta, \nu_a)$  and the factor  $\left( \frac{\partial B}{\partial T} \right)_{\nu_a}$  all vary with the frequency  $\nu_a$  in eq. (31). However, for the present analysis we only consider the frequency dependence of the HI signal  $\delta T(\theta, \nu_a)$  which is assumed to vary much more rapidly with  $\nu_a$  in comparison to the other terms which are expected to have a relatively slower frequency dependence which has been ignored here. We then have

$$\mathcal{S}(\mathbf{U}_i, \nu_a) = \left( \frac{\partial B}{\partial T} \right) \int d^2U \tilde{a}(\mathbf{U}_i - \mathbf{U}) \Delta \tilde{T}(\mathbf{U}, \nu_a), \quad (33)$$

which is similar to eq. (3) introduced earlier.

In eq. (33), we can express  $\Delta \tilde{T}(\mathbf{U}, \nu)$  in terms of  $\Delta T(\mathbf{k})$  which refers to the three dimensional (3D) Fourier decomposition of the HI brightness temperature fluctuations in the region of space from which the redshifted 21 cm radiation originated. We use equation (7) of Bharadwaj & Sethi (2001) (or equivalently eq. (12) of Bharadwaj & Ali (2005)) to express  $\mathcal{S}(\mathbf{U}_i, \nu)$  in terms of the three dimensional brightness temperature fluctuations

$$\mathcal{S}(\mathbf{U}_i, \nu) = \left( \frac{\partial B}{\partial T} \right) \int \frac{d^3k}{(2\pi)^3} \tilde{a} \left( \mathbf{U}_i - \frac{\mathbf{k}_\perp r}{2\pi} \right) e^{-ik_\parallel r'} \nu \Delta \tilde{T}(\mathbf{k}), \quad (34)$$

where  $(\mathbf{k}_\perp, k_\parallel)$  are the components of the comoving wave vector  $\mathbf{k}$  respectively perpendicular and parallel to the line of sight,  $r$  is the comoving distance corresponding to the redshifted 21-cm radiation at the observing frequency  $\nu$ ,  $r' = |dr/d\nu|$ , and

$$\langle \Delta \tilde{T}(\mathbf{k}) \Delta \tilde{T}^*(\mathbf{k}') \rangle = (2\pi)^3 \delta_D^3(\mathbf{k} - \mathbf{k}') P(\mathbf{k}_\perp, k_\parallel) \quad (35)$$

defines  $P(\mathbf{k}_\perp, k_\parallel)$ , the 3D power spectrum of HI brightness temperature fluctuations.  $\nu$  here is measured with respect to the central frequency of the observation, and  $r$  and  $r'$  are held fixed at the values corresponding to the central frequency.

We next consider observations with  $N_c$  discrete frequency channels  $\nu_a$  with  $a = 0, 1, 2, \dots, N_c - 1$ , each channel of width  $\Delta\nu_c$  and the total spanning a frequency bandwidth  $B_{\text{bw}}$ . This corresponds to a comoving spatial extent of  $(r' B_{\text{bw}})$  along the line of sight and  $k_\parallel$  now assumes discrete values

$$k_\parallel = \frac{2\pi \tau_m}{r'} \quad (36)$$



where  $\tau_m$  is the delay variable (Morales & Hewitt 2004; McQuinn et al. 2006) which takes values  $\tau_m = m/B_{\text{bw}}$  with  $-N_c/2 < m \leq N_c/2$ . The  $k_{\parallel}$  integral in eq. (34) is now replaced by a discrete sum  $\int k_{\parallel}/(2\pi) \rightarrow (r' B_{\text{bw}})^{-1} \sum_m$ . It is further convenient to use

$$\mathbf{k}_{\perp} = \frac{2\pi\mathbf{U}}{r} \quad (37)$$

whereby

$$\mathcal{S}(\mathbf{U}_i, \nu_a) = \left( \frac{\partial B}{\partial T} \right) \int d^2U \tilde{a}(\mathbf{U}_i - \mathbf{U}) \sum_m e^{-2\pi i \tau_m \nu_a} \frac{\Delta \tilde{T}(\mathbf{U}, \tau_m)}{B_{\text{bw}} r^2 r'}. \quad (38)$$

Note here that we can identify  $\tau_m$  as being the Fourier conjugate of  $\nu_a$ .

We now consider the Fourier transform along the frequency axis of the measured visibilities which gives the visibilities  $v_i(\tau_m)$  in delay space

$$v_i(\tau_m) = (\Delta \nu_c) \sum_a e^{2\pi i \tau_m \nu_a} \mathcal{V}_i(\nu_a). \quad (39)$$

The subsequent analysis of this section is entirely based on the delay space visibilities  $v_i(\tau_m)$  defined in eq. (39).

Calculating  $s(\mathbf{U}_i, \tau_m)$ , the HI signal contribution to  $v_i(\tau_m)$  using eq. (38), we have

$$s(\mathbf{U}_i, \tau_m) = \left( \frac{\partial B}{\partial T} \right) \int d^2U \tilde{a}(\mathbf{U}_i - \mathbf{U}) \left[ \frac{\Delta \tilde{T}(\mathbf{U}, \tau_m)}{r^2 r'} \right], \quad (40)$$

where rewriting eq. (35) in terms of the new variables  $\mathbf{U}$  and  $\tau_m$  we have

$$\langle \Delta \tilde{T}(\mathbf{U}, \tau_m) \Delta \tilde{T}^*(\mathbf{U}, \tau_n) \rangle = \delta_D^2(\mathbf{U} - \mathbf{U}') \left[ \delta_{m,n} (B_{\text{bw}} r^2 r') P(\mathbf{k}_{\perp}, k_{\parallel}) \right]. \quad (41)$$

We see that the signal at two different delay channels is uncorrelated. It is straight forward to also verify that the noise contribution  $n_i(\tau_m)$  at two different delay channels is uncorrelated.

In summary of the calculations discussed till now in this section, we see that the visibilities  $v_i(\tau_m)$  at two different delay channels are uncorrelated. It therefore suffices to individually analyze each delay channel separately, and in the subsequent discussion we restrict our attention to a fixed delay channel  $\tau_m$ . Calculating the correlation of a visibility with itself, we have

$$\langle |v_i(\tau_m)|^2 \rangle = V_0 \left[ \frac{B_{\text{bw}}}{r^2 r'} P(\mathbf{k}_{\perp}, k_{\parallel}) \right] + (\Delta \nu_c)^2 \sum_a \langle |\mathcal{N}_i(\nu_a)|^2 \rangle. \quad (42)$$

It is important to note that eqs. (40), (41) and (42) which hold for a fixed delay channel are exactly analogous to eqs. (3), (4) and (7) which hold for a fixed frequency channel. We define the convolved visibilities in exact analogy with eq. (9)

$$v_{cg}(\tau_m) = \sum_i \tilde{w}(\mathbf{U}_g - \mathbf{U}_i) v_i(\tau_m), \quad (43)$$

and we define the 3D TGE in exact analogy with eq. (17).

$$\hat{P}_g(\tau_m) = \left( \frac{M_g B_{\text{bw}}}{r^2 r'} \right)^{-1} \left( |v_{cg}(\tau_m)|^2 - \sum_i |\tilde{w}(\mathbf{U}_g - \mathbf{U}_i)|^2 |v_i(\tau_m)|^2 \right). \quad (44)$$

The 3D TGE is, by construction, an unbiased estimator of the three dimensional power spectrum  $P(\mathbf{k}_{\perp}, k_{\parallel})$ , and we have

$$\langle \hat{P}_g(\tau_m) \rangle = P(\mathbf{k}_{\perp g}, k_{\parallel m}) \quad (45)$$

where  $k_{\parallel m}$  and  $\mathbf{k}_{\perp g}$  are related to  $\tau_m$  and  $\mathbf{U}_g$  through eqs. (36) and (37) respectively.

### 3.2 Frequency Window Function

The discrete Fourier transform used to calculate  $v_i(\tau_m)$  in eq. (39) assumes that the measured visibilities  $\mathcal{V}_i(\nu_a)$  are periodic across the frequency bandwidth  $B_{\text{bw}}$  (*i.e.*  $\mathcal{V}_i(\nu_a) = \mathcal{V}_i(\nu_a + B_{\text{bw}})$ ). In reality, the measured visibilities are not periodic over the observational bandwidth, and the discrete Fourier transform encounters a discontinuity at the edge of the band. It is possible to avoid this problem by multiplying the measured visibilities with a frequency window function  $F(\nu_a)$  which smoothly falls to zero at the edges of the band. This effectively makes the product  $F(\nu_a) \times \mathcal{V}_i(\nu_a)$  periodic, thereby doing away with the discontinuity at the edges of the band. This issue has been studied by Vedantham et al. (2012) and Thyagarajan et al. (2013) who have proposed the Blackman-Nuttall (Nuttall 1981) window function

$$F(a) = c_0 - c_1 \cos\left(\frac{2\pi a}{N_c - 1}\right) + c_2 \cos\left(\frac{4\pi a}{N_c - 1}\right) - c_3 \cos\left(\frac{6\pi a}{N_c - 1}\right) \quad (46)$$

where  $c_0 = 0.3635819$ ,  $c_1 = 0.4891775$ ,  $c_2 = 0.1365995$  and  $c_3 = 0.0106411$ . In a recent paper, Chapman et al. (2014) have compared different frequency window functions to conclude that the extended Blackman-Nuttall window is the best choice for recovering the HI power spectrum. For the present work we have used the Blackman-Nuttall window as given by eq. (46) above. The left panel of Figure 4 shows the frequency window function for 256 frequency channels spanning a frequency bandwidth of  $B_{\text{bw}} = 16$  MHz which corresponds to the values which we have used in our simulations (discussed later).

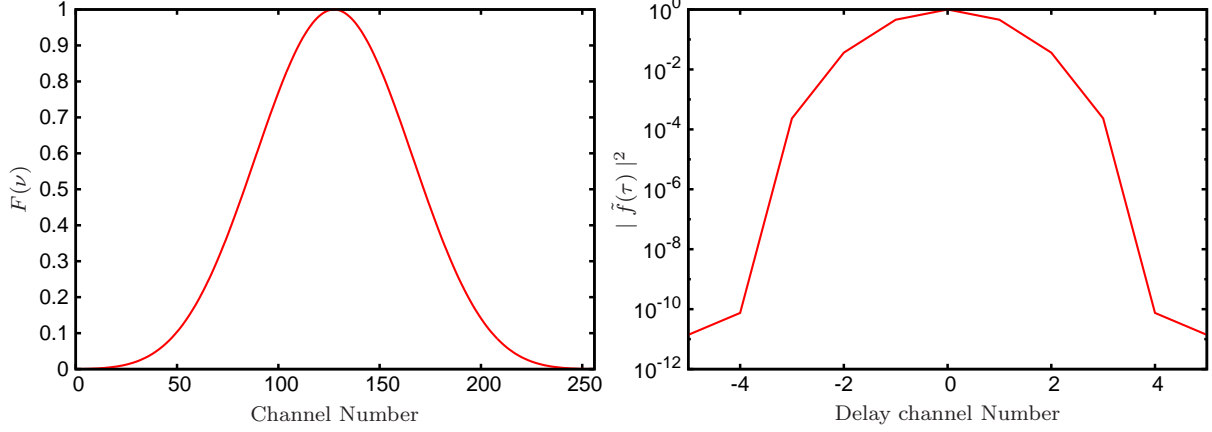


**Figure 4.** The Blackman-Nuttall frequency window  $F(\nu)$  as a function of channel number is shown in the left panel. The right panel shows  $(|\tilde{f}(\tau)|^2)$  which is the square of the Fourier transform of  $F(\nu)$ . This is normalized to unity at the central delay channel.

We now have

$$v_i^f(\tau_m) = (\Delta\nu_c) \sum_a e^{2\pi i\tau_m\nu_a} F(\nu_a) \mathcal{V}_i(\nu_a) \quad (47)$$

where  $v_i^f(\tau_m)$  refer to the delay space visibilities after introducing the frequency window function. The filtered delay space visibilities  $v_i^f(\tau_m)$  are related to the original delay space visibilities  $v_i(\tau_m)$  (eq. (39)) through a convolution

$$v_i^f(\tau_m) = \frac{1}{B_{\text{bw}}} \sum_n \tilde{f}(\tau_m - \tau_n) v_i(\tau_n) \quad (48)$$

where  $\tilde{f}(\tau)$  is the Fourier transform of the frequency window  $F(\nu)$ . Recollect that the delay space visibilities  $v_i(\tau_m)$  at the different  $\tau_m$  are all independent and uncorrelated. We however see that this does not hold for the filtered delay space visibilities  $v_i^f(\tau_m)$  for which the different  $\tau_m$  values are correlated, the extent of this correlation being determined by the width of the function  $\tilde{f}(\tau_m - \tau_n)$  in eq. (48). We now use this to calculate the correlation of  $v_i^f(\tau_m)$  at two different values of  $\tau_m$  for which we have

$$\langle v_i^f(\tau_m) v_i^{f*}(\tau_n) \rangle = \frac{1}{B_{\text{bw}}^2} \sum_a \tilde{f}(\tau_m - \tau_a) \tilde{f}^*(\tau_n - \tau_a) \langle |v_i(\tau_a)|^2 \rangle. \quad (49)$$

This gives the self-correlation to be

$$\langle |v_i^f(\tau_m)|^2 \rangle = \frac{1}{B_{\text{bw}}^2} \sum_a |\tilde{f}(\tau_m - \tau_a)|^2 \langle |v_i(\tau_a)|^2 \rangle. \quad (50)$$

The right panel of Figure 4 show  $|\tilde{f}(\tau_m)|^2$  as a function of the delay channel number  $m$ . We see that  $|\tilde{f}(\tau_m)|^2$  has a very narrow extent in delay space, implying that the visibilities  $v_i^f(\tau_m)$  in only three adjacent delay channels are correlated, and  $v_i^f(\tau_m)$  are uncorrelated if the delay channel separation is larger than this. This also allows us to approximate  $|\tilde{f}(\tau_m - \tau_n)|^2$  using a Kronecker delta function  $\approx B_{\text{bw}}^2 A_f(0) \delta_{m,n}$  where  $A_f(0) = \frac{1}{B_{\text{bw}}^2} \sum_n |\tilde{f}(\tau_n)|^2$ . The convolution in eq. (50) now gives

$$\langle |v_i^f(\tau_m)|^2 \rangle = A_f(0) \langle |v_i(\tau_m)|^2 \rangle. \quad (51)$$

We now generalize this to calculate the correlation for two different values of  $\tau_m$  which gives

$$\langle v_i^f(\tau_m) v_i^{f*}(\tau_n) \rangle = A_f(m-n) \langle |v_i(\tau_m)|^2 \rangle \quad (52)$$

where

$$A_f(m-n) = \frac{1}{B_{\text{bw}}^2} \sum_a \tilde{f}(\tau_m - \tau_a) \tilde{f}^*(\tau_n - \tau_a) \quad (53)$$

and  $A_f(m-n) = A_f^*(n-m)$ . We find that  $A_f(m)$  has significant values only for  $m = 0, 1, 2, 3$  beyond which the values are rather small *i.e.* the visibilities at only the three adjacent delay channels have significant correlations, and the visibilities are uncorrelated beyond this separation. We have used the self-correlation (eq. 51) to calculate the power spectrum estimator later in this subsection, whereas the general expression for the correlation (eq. 52) comes in useful for calculating the variance in a subsequent subsection.

Incorporating the frequency window function in the 3D TGE introduces an additional factor of  $A_f(0)$  in the normalization

coefficient in eq. (44). We now have the final expression for the 3D TGE as

$$\hat{P}_g(\tau_m) = \left( \frac{M_g B_{bw} A_f(0)}{r^2 r'} \right)^{-1} \left( |v_{cg}^f(\tau_m)|^2 - \sum_i |\tilde{w}(\mathbf{U}_g - \mathbf{U}_i)|^2 |v_i^f(\tau_m)|^2 \right). \quad (54)$$

As mentioned earlier,  $\hat{P}_g(\tau_m)$  gives an estimate of the power spectrum  $P(\mathbf{k}_{\perp g}, k_{\parallel m})$  where  $k_{\parallel m}$  and  $\mathbf{k}_{\perp g}$  are related to  $\tau_m$  and  $\mathbf{U}_g$  through eqs. (36) and (37) respectively.

### 3.3 Binning and Variance

The estimator  $\hat{P}_g(\tau_m)$  presented in eq. (54) provides an estimate of the 3D power spectrum  $P(\mathbf{k}_{\perp g}, k_{\parallel m})$  at an individual grid point  $\mathbf{k} = (\mathbf{k}_{\perp g}, k_{\parallel m})$  in the three dimensional  $\mathbf{k}$  space. Usually one would like to average the estimated power spectrum over a bin in  $\mathbf{k}$  space in order to increase the signal-to-noise ratio. In this section we discuss the bin averaged 3D TGE and obtain formulas for theoretically predicting the expected variance.

We introduce the binned 3D TGE which for the bin labeled  $a$  is defined as

$$\hat{P}_G(a) = \frac{\sum_{gm} w_{gm} \hat{P}_g(\tau_m)}{\sum_{gm} w_{gm}} \quad (55)$$

where the sum is over all the  $\mathbf{k} = (\mathbf{k}_{\perp g}, k_{\parallel m})$  modes or equivalently the grid points  $(\mathbf{U}_g, \tau_m)$  included in the particular bin  $a$ , and  $w_{gm}$  is the weight assigned to the contribution from any particular grid point. Earlier in this paper, in the discussion just subsequent to eq. (19), we have introduced the weighing scheme  $w_g = 1$  in order to calculate  $C_\ell$ . Here we have adopted the same scheme  $w_{gm} = 1$  for estimating the 3D power spectrum.

The expectation value of the binned 3D TGE (eq. 55)

$$\langle \hat{P}_G(a) \rangle = \bar{P}(\bar{k}_\perp, \bar{k}_\parallel)_a \quad (56)$$

gives an estimate of the bin averaged 3D power spectrum

$$\bar{P}(\bar{k}_\perp, \bar{k}_\parallel)_a = \frac{\sum_{gm} w_{gm} P(\mathbf{k}_{\perp g}, k_{\parallel m})}{\sum_{gm} w_{gm}} \quad (57)$$

at

$$(\bar{k}_\perp, \bar{k}_\parallel)_a = \left( \frac{\sum_{gm} w_{gm} k_{\perp g}}{\sum_{gm} w_{gm}}, \frac{\sum_{gm} w_{gm} k_{\parallel m}}{\sum_{gm} w_{gm}} \right). \quad (58)$$

where for the particular bin  $a$  the two components  $(\bar{k}_\perp, \bar{k}_\parallel)_a$  refer to the average wave numbers respectively perpendicular and parallel to the line of sight. In this paper we have considered two different binning schemes which we discuss later in this sub-section. For the present, we turn our attention to calculate theoretical predictions for the variance of the binned 3D TGE.

The variance calculation closely follows the steps outlined in section 2.4, and we have the final expression

$$\sigma_{P_G}^2 = \left( \frac{B_{bw} A_f(0)}{r^2 r'} \right)^{-2} \frac{\sum_{gm, g'm'} w_{gm} w_{g'm'} M_g^{-1} M_{g'}^{-1} |\langle v_{cg}^f(\tau_m) v_{cg'}^{f*}(\tau_{m'}) \rangle|^2}{[\sum_{gm} w_{gm}]^2}. \quad (59)$$

which closely resembles eq. (25) which we have used to calculate the variance for  $C_\ell$ , with the difference that we now have a 3D grid instead of the 2D grid encountered earlier for  $C_\ell$ .

It is necessary to model the term  $\langle v_{cg}^f(\tau_m) v_{cg'}^{f*}(\tau_{m'}) \rangle$  in eq. (59) to make further progress. The correlation at two different  $\tau_m$  values can be expressed using eq. (52) as

$$\langle v_{cg}^f(\tau_m) v_{cg'}^{f*}(\tau_{m'}) \rangle = A_f(m - m') \langle v_{cg}(\tau_m) v_{cg'}^*(\tau_{m'}) \rangle. \quad (60)$$

Following eq. (26), we have decomposed the correlation  $\langle v_{cg}(\tau_m) v_{cg'}^*(\tau_{m'}) \rangle$  in eq. (60) into two parts

$$\langle v_{cg}(\tau_m) v_{cg'}^*(\tau_{m'}) \rangle = \langle s_{cg}(\tau_m) s_{cg'}^*(\tau_{m'}) \rangle + \langle n_{cg}(\tau_m) n_{cg'}^*(\tau_{m'}) \rangle \quad (61)$$

corresponding to the signal and the noise respectively.

We have modeled the signal correlation in exact analogy with eq. (27) as

$$\langle s_{cg}(\tau_m) s_{cg'}^*(\tau_{m'}) \rangle = \left( \frac{B_{bw}}{r^2 r'} \right) \sqrt{M_g M_{g'}} e^{-|\Delta \mathbf{U}_{gg'}|^2 / \sigma_1^2} \bar{P}(\bar{k}_\perp, \bar{k}_\parallel)_a \quad (62)$$

and the noise correlation is similarly modeled in exact analogy with eq. (29) as

$$\langle n_{cg}(\tau_m) n_{cg'}^*(\tau_{m'}) \rangle = (\Delta \nu_c) B_{bw} \sqrt{K_{2gg} K_{2g'g'}} e^{-|\Delta \mathbf{U}_{gg'}|^2 / \sigma_2^2} (2\sigma_n^2). \quad (63)$$

We have used eqs. (63), (62), (61), (60) and (59) to calculate the variance of the binned 3D TGE. In the subsequent analysis we have considered two different binning schemes which we now present below.

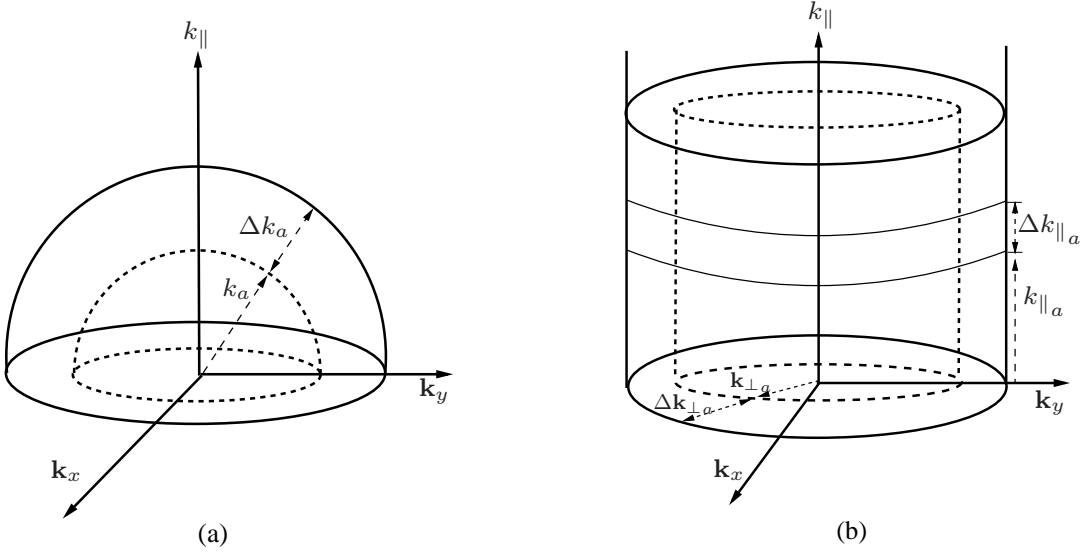


**Figure 5.** This shows a typical bin for respectively calculating the Spherical Power Spectrum (left) and the Cylindrical Power Spectrum (right).

### 3.3.1 1D Spherical Power Spectrum

The bins here are spherical shells of thickness  $\Delta k_a$  as shown in the left panel of Figure 5, the shell thickness will in general vary from bin to bin. The Spherical Power Spectrum  $\bar{P}(\bar{k}_a)$  is obtained by averaging the power spectrum  $P(\mathbf{k})$  over all the different  $\mathbf{k}$  modes which lie within the spherical shell corresponding to bin  $a$  shown in the left panel of Figure 5. The binning here essentially averages out any anisotropy in the power spectrum, and yields the bin averaged power spectrum as a function of the 1D bin averaged wave number  $\bar{k}_a$ . While we use eq. (55) to calculate the bin averaged power spectrum  $\bar{P}(\bar{k}_a)$ , we have calculated the value of  $\bar{k}_a$  using

$$\bar{k}_a = \frac{\sum_{gm} w_{gm} \sqrt{k_{\perp g}^2 + k_{\parallel m}^2}}{\sum_{gm} w_{gm}}. \quad (64)$$

### 3.3.2 2D Cylindrical Power Spectrum

Each bins here is, as shown in the right panel of Figure 5, an annulus of width  $\Delta k_{\perp a}$  in the  $\mathbf{k}_{\perp} \equiv (k_x, k_y)$  plane and it subtends a thickness  $\Delta k_{\parallel a}$  along the third direction  $k_{\parallel}$ . The values of  $\Delta k_{\perp a}$  and  $\Delta k_{\parallel a}$  will, in general, vary from bin to bin. The bins here correspond to sections of a hollow cylinder, and the resulting bin averaged power spectrum  $\bar{P}(\bar{k}_{\perp}, \bar{k}_{\parallel})_a$  is referred to as the Cylindrical Power Spectrum which is defined on a 2D space  $(\bar{k}_{\perp}, \bar{k}_{\parallel})_a$  whose two components refer to the average wave numbers respectively perpendicular and parallel to the line of sight. The binning of  $P(\mathbf{k})$  here does not assume that the signal is statistically isotropic in the 3D space *i.e.* independent of the direction of  $\mathbf{k}$ . However, the signal is assumed to be statistically isotropic in the plane of the sky, and the binning in  $\mathbf{k}_{\perp}$  is exactly identical to the binning that we have used earlier for  $C_{\ell}$ . This distinction between  $k_{\perp}$  and  $k_{\parallel}$  is useful to quantify the effect of redshift space distortion (Bharadwaj, Nath and Sethi 2001; Bharadwaj & Sethi 2001; Bharadwaj & Ali 2004; Barkana & Loeb 2005; Mao 2012; Majumdar, Bharadwaj & Choudhuri 2013; Jensen et al. 2016) and also to distinguish the foregrounds from the HI signal (Morales & Hewitt 2004). We have used eq. (55) and eq. (58) to calculate  $\bar{P}(\bar{k}_{\perp}, \bar{k}_{\parallel})_a$  and  $(\bar{k}_{\perp}, \bar{k}_{\parallel})_a$  respectively.

## 4 SIMULATION

In this section we discuss the simulations that we have used to validate the 3D power spectrum estimator (eq. 54). We start with an input model 3D power spectrum  $P^M(k)$  of redshifted HI 21-cm brightness temperature fluctuations. The aim here is to test how well the estimator is able to recover the input model. For this purpose the exact form of the input model power spectrum need not mimic the expected cosmological HI signal, and we have used a simple power law

$$P^M(k) = \left(\frac{k}{k_0}\right)^n \quad (65)$$

which is arbitrarily normalized to unity at  $k = k_0$ , and has a power law index  $n$ . In our analysis we have considered  $n = -3$  and  $-2$ , and set  $k_0 = 1 \text{ Mpc}^{-1}$ . The quantity  $\Delta_k^2 = (2\pi^2)^{-1} k^3 P(k)$  provides an estimate of the mean-square brightness

temperature fluctuations expected at different length-scales (or equivalently wave numbers  $k$ ). We see that for  $n = -3$  we have a constant  $\Delta_k^2 = (2\pi^2)^{-1} \text{K}^2$  across all length-scales, whereas we have  $\Delta_k^2 = (2\pi^2)^{-1} (k/1 \text{Mpc}^{-1}) \text{K}^2$  which increases linearly with  $k$  for  $n = -2$ . Note that we have used an isotropic input model where the power spectrum does not depend on the direction of  $\mathbf{k}$  *i.e.* ( $P(\mathbf{k}) \equiv P(k)$ ) and the 1D Spherical binning and the 2D Cylindrical binning are expected to recover the same results.

The simulations were carried out using a  $N^3$  cubic grid of spacing  $L$  covering a comoving volume  $V$ . We use the model power spectrum (eq. 65) to generate the Fourier components of the brightness temperature fluctuations corresponding to this grid

$$\Delta\tilde{T}(\mathbf{k}) = \sqrt{\frac{VP^M(k)}{2}} [a(\mathbf{k}) + ib(\mathbf{k})], \quad (66)$$

here  $a(\mathbf{k})$  and  $b(\mathbf{k})$  are two real valued independent Gaussian random variable of unit variance. The Fourier transform of  $\Delta T(\mathbf{k})$  yields a single realization of the brightness temperature fluctuations  $\delta T(\vec{x})$  on the simulation grid. These fluctuations are, by construction, a Gaussian random field with power spectrum  $P^M(k)$ . We generate different statistically independent realizations of  $\delta T(\vec{x})$  by using different sets of random variables  $a(\mathbf{k})$  and  $b(\mathbf{k})$  in eq. (66).

The intention here is to simulate 150 MHz GMRT observations with  $N_c = 256$  frequency channels of width ( $\Delta\nu_c$ ) = 62.5 kHz covering a bandwidth of  $B_{\text{bw}} = 16$  MHz. This corresponds to HI at redshift  $z = 8.47$  with a comoving distance of  $r = 9.28$  Gpc and  $r' = |dr/d\nu| = 17.16 \text{Mpc MHz}^{-1}$ . We have chosen the grid spacing  $L = 1.073$  Mpc so that it exactly matches the channel width  $L = r'_\nu \times (\Delta\nu_c)$ . We have considered a  $N^3 = [2048]^3$  grid which corresponds to a comoving volume of  $[2197.5 \text{Mpc}]^3$ . The simulation volume is aligned with the  $z$  axis along the line of sight, and the two transverse directions were converted to angles relative to the box center  $(\theta_x, \theta_y) = (x/r, y/r)$ . The transverse extent of the simulation box covers an angular extent which is  $\sim 5$  times the GMRT  $\theta_{FWHM}$ . The simulation volume corresponds to a frequency width  $\sim 8 \times 16$  MHz along the line of sight. We have cut the box into 8 equal segments along the line of sight to produce 8 independent realizations each subtending 16 MHz along the line of sight. The grid index, measured from the further boundary and increasing towards to observer along the line of sight was directly converted to channel number  $\nu_a$  with  $a = 0, 1, 2, \dots, N_c - 1$ . This procedure provides us with  $\delta T(\theta, \nu_a)$  the brightness temperature fluctuation on the sky at different frequency channels  $\nu_a$ .

We have considered 8 hours of GMRT observations with 16 s integration time targeted on an arbitrarily selected field located at RA=10h 46m 00s and DEC=59° 00' 59". Visibilities were calculated for the simulated baselines corresponding to this observation, for which the  $uv$  coverage is similar to the Figure 5 of Paper I. The signal contribution to the visibilities  $\mathcal{S}(\mathbf{U}, \nu_a)$  was calculated by taking the Fourier transform of the product  $(\frac{\partial B}{\partial T}) \times \mathcal{A}(\theta, \nu_a) \times \delta T(\theta, \nu_a)$  as given by eq. (31). The simulations incorporate the fact that the baseline corresponding to a fixed antenna separation  $\mathbf{U}_i = \mathbf{d}_i/\lambda$ , the antenna beam pattern  $\mathcal{A}(\theta, \nu_a)$  and the factor  $(\frac{\partial B}{\partial T})_{\nu_a}$  all vary with the frequency  $\nu_a$  in eq. (31). We have  $\sigma_n = 1.45$  Jy corresponding to a single polarization, with  $\Delta t = 16$  s and  $(\Delta\nu_c) = 62.5$  kHz. However, it is possible to reduce noise level by averaging independent data set observed at different time. Here, we consider a situation where we average 9 independent data sets to reduce the noise level by a factor of 3 to  $\sigma_n = 0.48$  Jy. We have carried out the simulations for two different cases, (i) no noise ( $\sigma_n = 0$  Jy) and (ii)  $\sigma_n = 0.48$  Jy. We have carried out 16 independent realization of the simulated visibilities to estimate the mean power spectrum and its statistical fluctuation (or standard deviation  $\sigma_{P_G}$ ) presented in the next section.

## 5 RESULTS

The left panels of Figures 6 and 7 show  $\Delta_k^2 = (2\pi^2)^{-1} k^3 P(k)$  for the spherically-averaged power spectrum for the power law index values  $n = -3$  and  $-2$  respectively. The results are shown for the three values  $f = 10, 2$  and  $0.6$  to demonstrate the effect of varying the tapering. The simulations here do not include the system noise contribution. For both  $n = -3$  and  $-2$ , and for all the values of  $f$  we find that  $\Delta_k^2$  estimated using the 3D TGE is within the  $1 - \sigma_{P_G}$  error bars of the model prediction for the entire  $k$  range considered here. The right panels of Figures 6 and 7 show the corresponding fractional deviations  $(P(k) - P^M(k))/P^M(k)$ . For comparison, the relative statistical fluctuations,  $\sigma_{P_G}/P^M(k)$  are also shown by shaded regions for different values of  $f$ . We find that for both cases  $n = -3$  and  $-2$ , the fractional deviation is less than 4% at  $k > 0.2 \text{Mpc}^{-1}$ . The fractional deviation increases as we go to lower  $k$  bins. The fractional deviation also increases if the value of  $f$  is reduced. The maximum fractional deviation has a value  $\sim 40\%$  and  $\sim 20\%$  at the smallest  $k$  bin for  $n = -3$  and  $-2$  respectively. We find that the fractional deviation is within  $\sigma_{P_G}/P^M(k)$  for  $k \leq 0.3 \text{Mpc}^{-1}$  and is slightly larger than  $\sigma_{P_G}/P^M(k)$  for  $k \geq 0.3 \text{Mpc}^{-1}$ . Our results indicate that the 3D TGE is able to recover the model power spectrum to a reasonably good level of accuracy ( $\leq 20\%$ ) at the  $k$  modes  $k \geq 0.1 \text{Mpc}^{-1}$ . The fractional error at the smaller  $k$  bins increases as the tapering is increased ( $f$  is reduced). It may be noted that a similar behaviour was also found for  $C_\ell$  (Figure 2). As mentioned earlier, we attribute this discrepancy to the variation of signal amplitude within the width of the convolving window  $\tilde{w}(\mathbf{U}_g - \mathbf{U}_i)$ . This explanation is further substantiated by the fact that the fractional deviation is found to be larger for  $n = -3$  where the power spectrum is steeper compared to  $n = -2$ .

The results until now have not considered the effect of system noise. We now study how well the 3D TGE is able to

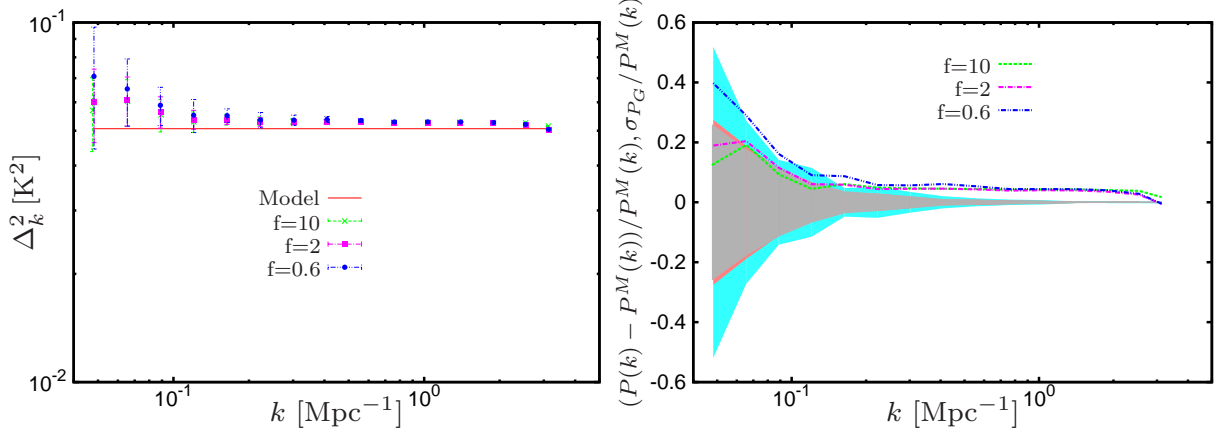


**Figure 6.** The left panel shows the dimensionless power spectrum  $\Delta_k^2$  for different values of  $f$ . The values obtained using the 3D TGE are compared with model power spectrum for  $n = -3$  and  $\sigma_n = 0$ . The  $1\text{-}\sigma_{PG}$  error bars have been estimated using 16 different realizations of the simulated visibilities. The right panel shows the fractional deviation of estimated power spectrum,  $(P(k) - P^M(k))/P^M(k)$  relative to the input model  $P^M(k)$  for different values of  $f$ . The relative statistical fluctuations  $\sigma_{PG}/P^M(k)$  are also shown by shaded regions.

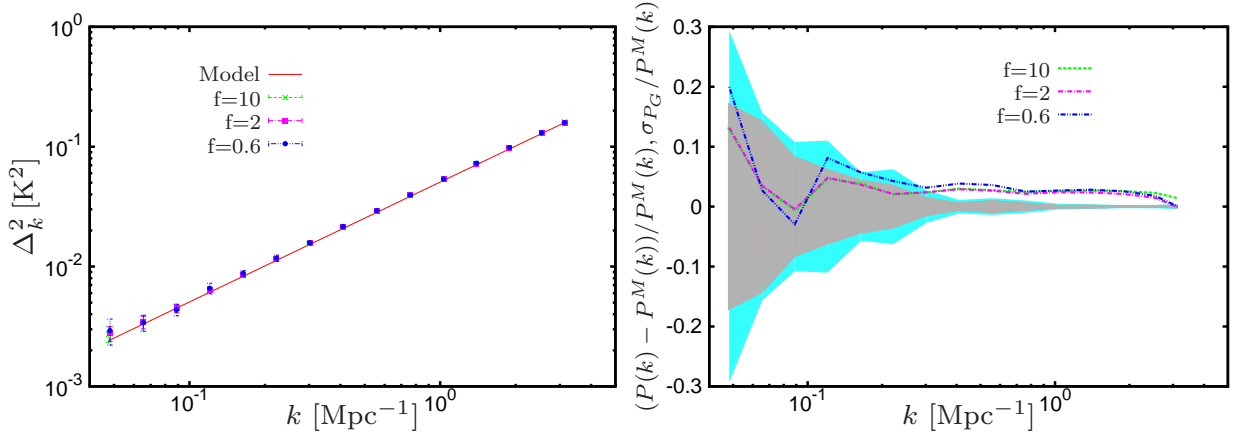


**Figure 7.** Same as Figure 6, but with  $n = -2$ .

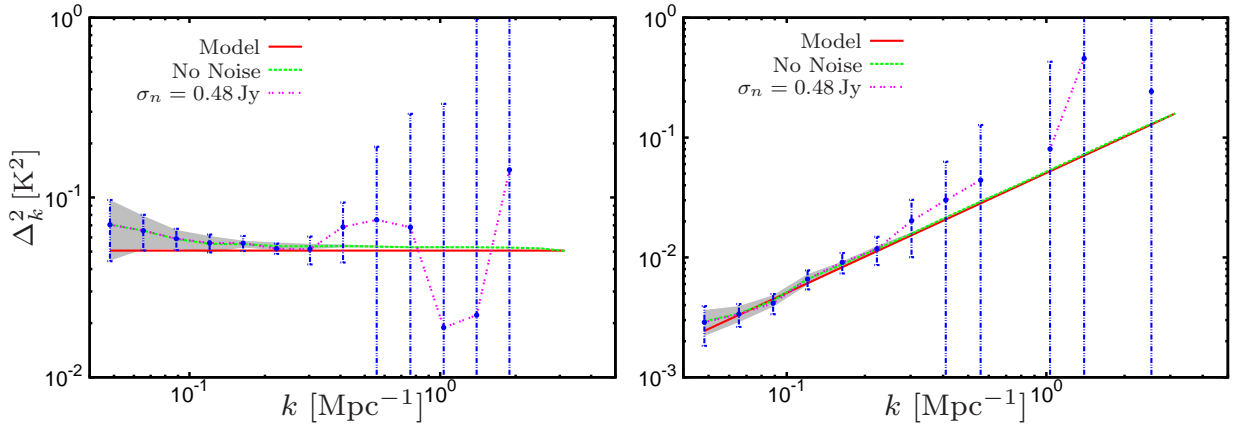


**Figure 8.** The recovered dimensionless power spectrum  $\Delta_k^2$  for  $n = -3$  (left) and  $n = -2$  (right), with and without noise for a fixed value  $f = 0.6$ . The statistical error ( $1\text{-}\sigma_{PG}$ ) with (without) noise is shown with error bars (shaded region). Note that, the estimated  $\Delta_k^2$  has negative values at some of the  $k$  values in the range where noise dominates the signal. These data points have not been displayed here.



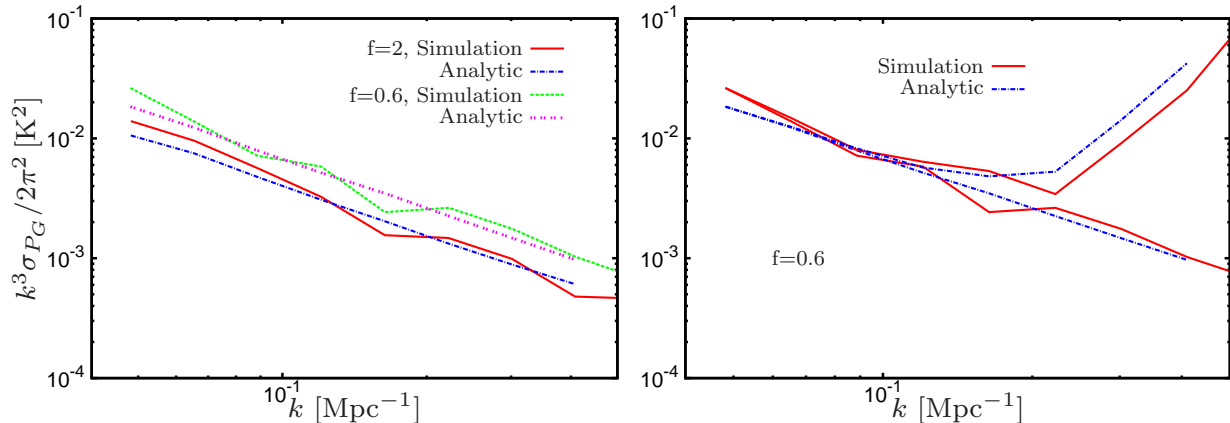


**Figure 9.** The left panel shows a comparison of the analytic prediction for the statistical fluctuations of the power spectrum (eq. 59) with the simulation for two different values of  $f$ ,  $n = -3$  and no system noise. The right panel shows the same comparison with (upper two curves) and without (lower two curves) noise for a fixed value  $f = 0.6$ .

recover the input power spectrum in the presence of system noise. The left and right panels of Figure 8 show the estimated  $\Delta_k^2$  for  $n = -3$  and  $-2$  respectively for the fixed value  $f = 0.6$ . For comparison, we also show the estimated  $\Delta_k^2$  with  $\sigma_n = 0$ . The statistical fluctuations with (without) noise are shown as error bars (shaded region). We see that the error is dominated by the cosmic variance at lower values of  $k$  ( $k < 0.2 \text{ Mpc}^{-1}$ ) and the system noise dominates at larger values of  $k$ . The statistical error exceeds the model power spectrum at large  $k$  and a statistically significant estimate of the power spectrum is not possible in this  $k$  range. We are able to recover the model power spectrum quite accurately at low  $k$  where  $\sigma_{P_G} \leq P^M(k)$ .

We now investigate how well the analytic prediction (eq. 59) for  $\sigma_{P_G}$  compares with the values obtained from the simulations (Figure 9) for different values of  $f$ . The number of grid points in each  $k$  bin increase with the value of  $k$ , and the computation also increases with increasing  $k$ . We have restricted the  $k$  range to ( $k < 0.4 \text{ Mpc}^{-1}$ ) in order to keep the computational requirements within manageable limits. In the left panel we consider the situation where there is no system noise. Here, the statistical fluctuations correspond to the cosmic variance. We see that the analytic predictions are in reasonably good agreement with the simulation for both the values of  $f$ . We find that the cosmic variance does not change if the value of  $f$  is changed from 2 to 10. As expected, the cosmic variance increases as the sky tapering is increased. The right panel shows the statistical fluctuations with and without noise for the fixed value  $f = 0.6$ . The statistical fluctuations are dominated by the cosmic variance at small values of  $k$  ( $k < 0.2 \text{ Mpc}^{-1}$ ), and the system noise dominates at large  $k$ . As mentioned earlier, the statistical fluctuations are well modeled by the analytic predictions in the cosmic variance dominated regime. We find that our analytic prediction somewhat overestimates  $\sigma_{P_G}$  in the noise dominated region. This overestimate possibly originates from the noise modelling in eq. (59), we plan to investigate this in future work.

Till now we have discussed the results for the 1D Spherical Power Spectrum, we now present the results for the 2D Cylindrical Power Spectrum. We use 15 equally spaced logarithmic bin in both  $k_\perp$  and  $k_\parallel$  direction to estimate the 2D Cylindrical Power Spectrum. Figure 10 shows the 2D Cylindrical Power Spectrum  $P(k_\perp, k_\parallel)$  using 3D TGE. The left panel shows the input model for  $n = -3$ . The middle and right panel respectively show the estimated power spectrum with  $f = 0.6$  for situations where the system noise is not included and included in the simulated visibilities. The left and middle panels appear almost indistinct indicating that the 3D TGE is able to recover the input model power spectrum accurately across the entire  $(k_\perp, k_\parallel)$  range. We find that we are able to recover the model power spectrum in the limited range  $k_\perp \lesssim 0.5 \text{ Mpc}^{-1}$  and  $k_\parallel \lesssim 0.5 \text{ Mpc}^{-1}$  in presence of system noise. Figure 11 shows the fractional deviation  $(P^M(k_\perp, k_\parallel) - P(k_\perp, k_\parallel))/P(k_\perp, k_\parallel)$  for  $f = 0.6$ , here the left and right panels show the results without and with system noise respectively. From the left panel we see that the fractional deviation is less than 14% for the the entire  $\mathbf{k}$  range when the system noise is not included in the simulation. We find that it is not possible to reliably recover the power spectrum at large  $\mathbf{k}$  when the system noise is included. In the right panel we have only shown the fractional deviation where it is within 30%, the values exceed 100% at large  $\mathbf{k}$  where the values have not been shown.

We now investigate how well the analytic prediction (eq. 59) for  $\sigma_{P_G}$  compares with the values obtained from the simulations (Figure 12) for  $f = 0.6$ . The two upper panels consider the situation where there is no system noise for which the left and right panels respectively show the simulated and the analytic prediction for the statistical fluctuation  $\sigma_{P_G}$ . We find that the analytic predictions match quite well with the simulation for the entire  $\mathbf{k}$  range. The two lower panels consider the situation where the system noise is included for which the left and right panels respectively show the simulated and the analytic prediction for  $\sigma_{P_G}$ . The left and right panels of Figure 13 show the fractional deviation between the simulated and analytic  $\sigma_{P_G}$  without and with system noise respectively. We find that we have less than 20% fractional deviation in 73% and

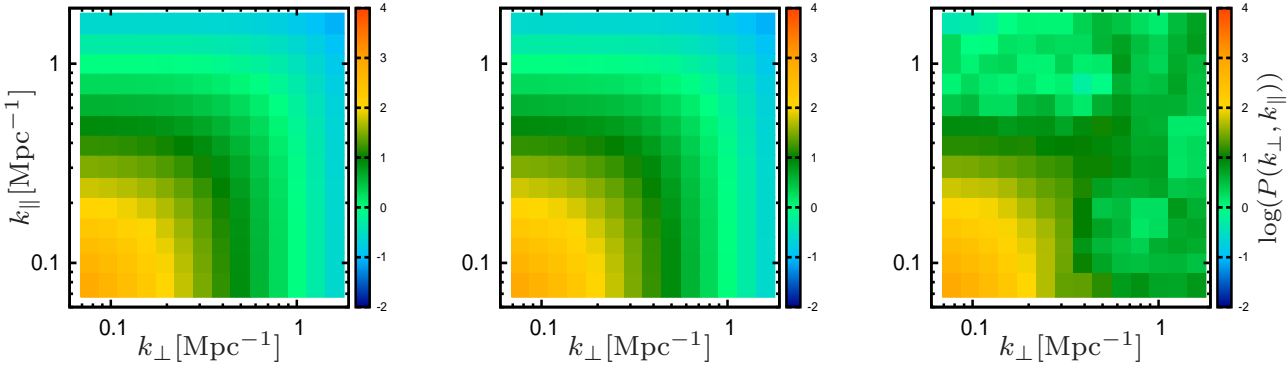


**Figure 10.** This shows the 2D Cylindrical Power Spectrum for  $n = -3$ . The left panel shows the input model power spectrum. The middle and right panels show the estimated power spectrum for  $f = 0.6$  without and with noise respectively.

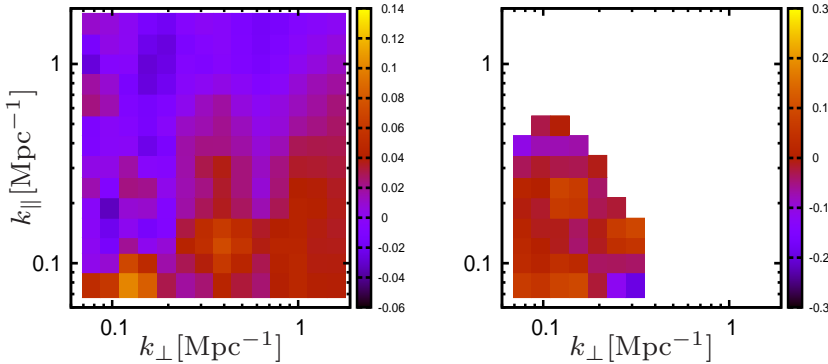


**Figure 11.** The left and right panels show the fractional deviation  $(P^M(k_\perp, k_\parallel) - P(k_\perp, k_\parallel))/P(k_\perp, k_\parallel)$  without and with noise respectively for  $n = -3$  and  $f = 0.6$ .

64% of the bins in  $(k_\perp, k_\parallel)$  space without and with system noise respectively. The fractional deviation shows a larger spread in values when the system noise is included as compared to the situation without system noise. We however do not find any obvious pattern in the distribution of the bins which show a high fractional deviation.

## 6 SUMMARY AND CONCLUSIONS

Quantifying the statistical properties of the diffuse sky signal directly from the visibilities measured in low frequency radio-interferometric observation is an important issue. In this paper we present a statistical estimator, namely the Tapered Gridded Estimator (TGE), which has been developed for this purpose. The measured visibilities are here gridded in the  $uv$  plane to reduce the complexity of the computation. The contribution from the discrete sources in the periphery of the telescope’s FoV, particularly the sidelobes, pose a problem for power spectrum estimation. The TGE suppresses the contribution from the outer regions by tapering the sky response through a suitably chosen window function. The TGE also internally estimates the noise bias from the input data, and subtracts this out to give an unbiased estimate of the power spectrum. In addition to the mathematical formalism for the estimator and its variance, we also present simulations of 150 MHz GMRT observations which are used to validate the estimator.

We have first considered a situation where we have observation at a single frequency for which the 2D TGE provides an estimate of the angular power spectrum  $C_\ell$ . The work here presents an improvement over an earlier version of the 2D TGE presented in Paper I. This is important in the context of the diffuse Galactic synchrotron emission which is one of the major

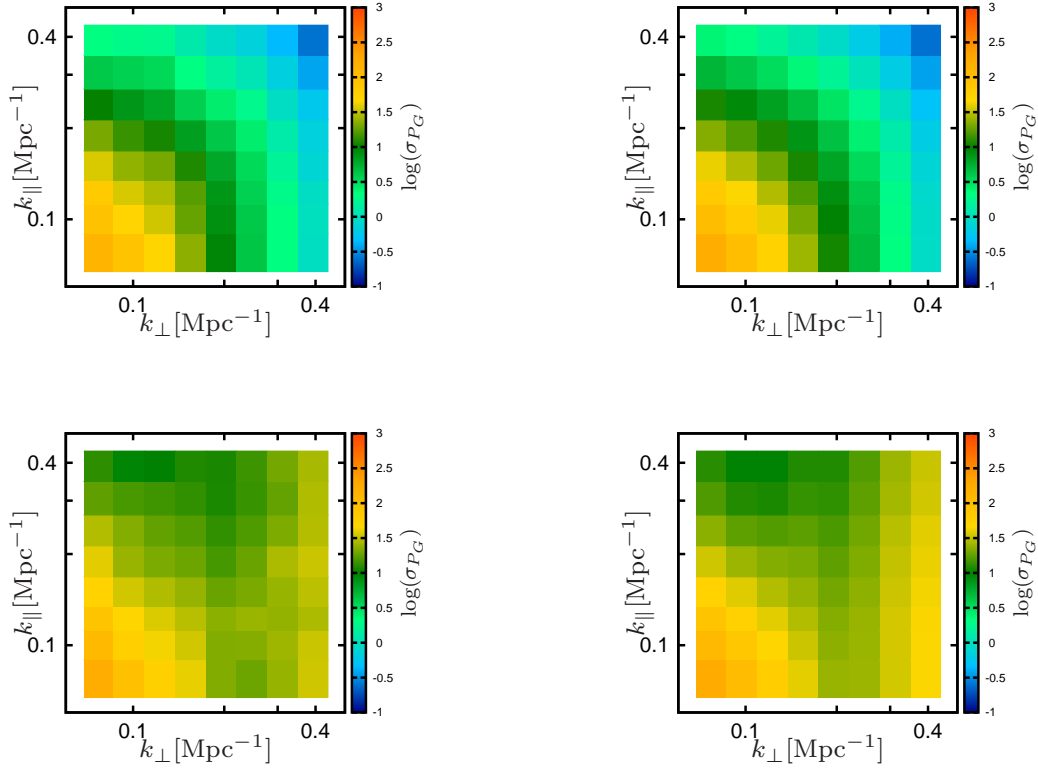


**Figure 12.** This shows the statistical fluctuation ( $\sigma_{PG}$ ) for the 2D Cylindrical Power Spectrum for  $n = -3$  and  $f = 0.6$ . The upper and lower panels show the results without and with system noise respectively, the left and right panels show the results from the simulations and the analytic prediction respectively.

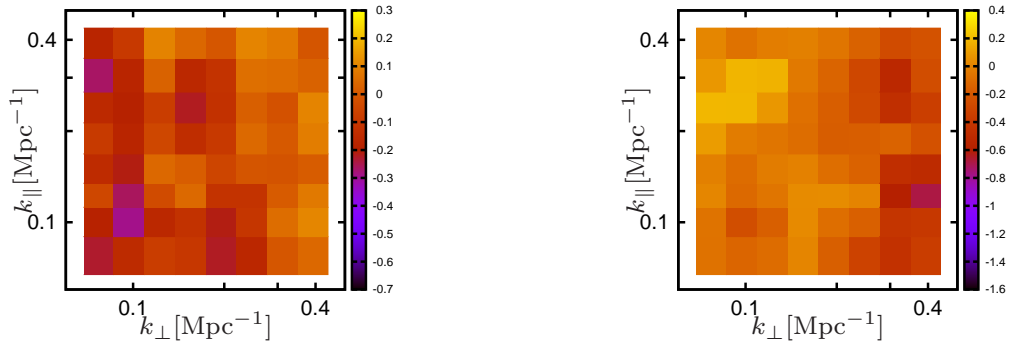


**Figure 13.** The left and right panels show the fractional deviation of  $\sigma_{PG}$  without and with system noise respectively.

foregrounds for the cosmological 21-cm signal. Apart from this, the diffuse Galactic synchrotron emission is a probe of the cosmic ray electrons and the magnetic fields in the ISM of our own Galaxy, and this is an important study in its own right.

It is necessary to also include the frequency variation of the sky signal in order to quantify the cosmological 21-cm signal. Here the 3D TGE provides an estimate of  $P(\mathbf{k})$  the power spectrum of the 21-cm brightness temperature fluctuations. We have considered two different binning schemes which provide the 1D Spherical Power Spectrum  $P(k)$  and the 2D Cylindrical Power Spectrum  $P(k_{\perp}, k_{\parallel})$  respectively. In all cases, we find that the TGE is able to accurately recover the input model used for the simulations. The analytic predictions for the variance are also found to be in reasonably good agreement with the simulations in most situations.

Foregrounds are possibly the biggest challenge for detecting the cosmological 21-cm power spectrum. Various studies (eg. Datta et al. 2010) show that the foreground contribution to the Cylindrical Power Spectrum  $P(k_{\perp}, k_{\parallel})$  is expected to be restricted within a wedge in the  $(k_{\perp}, k_{\parallel})$  plane. The extent of this “foreground wedge” is determined by the angular extent of the telescope’s FoV. In principle, it is possible to limit the extent of the foreground wedge by tapering the telescope’s FoV. In the context of estimating the angular power spectrum  $C_{\ell}$ , our earlier work (Paper II) has demonstrated that the 2D TGE is able to suppress the contribution from the outer parts and the sidelobes of the telescope’s beam pattern. We have not explicitly considered the foregrounds in our analysis of the 3D TGE presented in this paper. We however expect the 3D TGE to suppress the contribution from the outer parts and the sidelobes of the telescopes beam pattern while estimating the power spectrum  $P(k_{\perp}, k_{\parallel})$ , thereby reducing the area in the  $(k_{\perp}, k_{\parallel})$  plane under the foreground wedge.

The 3D TGE holds the promise of allowing us to reduce the extent of the foreground wedge by tapering the sky response. It is, however, necessary to note that this comes at a cost which we now discuss. First, we lose information at the largest angular scales due to the reduced FoV. This restricts the smallest  $k$  value at which it is possible to estimate the power spectrum. Second, the reduced FoV results in a larger cosmic variance for the smaller angular modes which are within the tapered FoV. The actual value of the tapering parameter  $f$  that would be used to estimate  $P(k_{\perp}, k_{\parallel})$  will possibly be determined by optimising between the cosmic variance and the foreground contribution. A possible strategy would be to use different values of  $f$  for different bins in the  $(k_{\perp}, k_{\parallel})$  plane. It is also necessary to note that the effectiveness of the tapering proposed here depends on the actual baseline distribution, and a reasonably dense  $uv$  coverage is required for a proper implementation of the TGE. We propose to include foregrounds in the simulations and address these issues in future work. We also plan to apply this estimator to 150 MHz GMRT data in future.

## 7 ACKNOWLEDGEMENTS

S. Choudhuri would like to acknowledge the University Grant Commission, India for providing financial support through Senior Research Fellowship. S. Chatterjee is supported by a University Grants Commission Research Fellowship. SSA would like to acknowledge C.T.S, I.I.T. Kharagpur for the use of its facilities and thank the authorities of the IUCAA, Pune, India for providing the Visiting Associateship programme.

## References

- Ali S. S., Bharadwaj S., & Chengalur J. N., 2008, MNRAS, 385, 2166A  
 Ali, S. S., & Bharadwaj, S. 2014, Journal of Astrophysics and Astronomy, 35,157  
 Ali, Z. S., Parsons, A. R., Zheng, H., et al. 2015, ApJ, 809, 61  
 Bandura K. et al., 2014, in Proc. SPIE, Vol. 9145, Ground-based and Airborne Telescopes V, p. 914522  
 Barkana, R., & Loeb, A. 2005, ApJL, 624, L65  
 Bernardi, G., de Bruyn, A. G., Brentjens, M. A., et al. 2009, A & A, 500, 965  
 Bharadwaj S., Nath B. & Sethi S.K. 2001, JApA, 22, 21  
 Bharadwaj , S. & Sethi , S. K., 2001 , JApA, 22 , 293  
 Bharadwaj, S., & Ali, S. S. 2004, MNRAS, 352, 142  
 Bharadwaj S. , & Ali S. S. 2005, MNRAS, 356, 1519  
 Bowman, J. D., Morales, M. F., & Hewitt, J. N. 2009, ApJ, 695, 183  
 Bowman J. D. et al., 2013, PASA, 30, e031  
 Bull, P, et al. 2015, ApJ, 803, 21  
 Chapman, E., Abdalla, F. B., Harker, G., et al. 2012, MNRAS, 423, 2518  
 Chapman, E., Zaroubi, S., Abdalla, F., et al. 2014, arXiv:1408.4695  
 Choudhuri, S., Bharadwaj, S., Ghosh, A., & Ali, S. S., 2014, MNRAS, 445, 4351  
 Choudhuri, S., Bharadwaj, S., Roy, N., Ghosh, A., & Ali, S. S., 2016, MNRAS, 459, 151  
 Datta, A., Bowman, J. D., & Carilli, C. L. 2010, ApJ, 724, 526  
 Dillon, J. S., Liu, A., Williams, C. L., et al. 2014, PRD, 89, 023002  
 Dillon, J. S., Liu, A., Williams, C. L., et al. 2015, PRD, 91(12), 123011  
 Di Matteo, T., Perna, R., Abel, T. & Rees, M.J., 2002, ApJ, 564, 576  
 Furlanetto S. R., Oh S. P., Briggs F. H., 2006, Phys. Rep.,433, 181  
 Ghosh, A., Bharadwaj, S., Ali, S. S., & Chengalur, J. N. 2011a, MNRAS, 411, 2426  
 Ghosh, A., Bharadwaj, S., Ali, S. S., & Chengalur, J. N. 2011b, MNRAS, 418, 2584  
 Ghosh, A., et al. 2012, MNRAS, 426, 3295  
 Iacobelli, M., Haverkorn, M., Orrú, E., et al. 2013, A & A, 558, A72  
 Jacobs, D. C., Hazelton, B. J., Trott, C. M., et al. 2016, arXiv:1605.06978

- Jelić, V., Zaroubi, S., Labropoulos, P., et al. 2008, *MNRAS*, 389, 1319
- Jensen, H., Majumdar, S., Mellema, G., et al. 2016, *MNRAS*, 456, 66
- Koopmans, L., Pritchard, J., Mellema, G., et al. 2015, *Advancing Astrophysics with the Square Kilometre Array (AASKA14)*, 1
- Liu, A., & Tegmark, M. 2012, *MNRAS*, 419, 3491
- Liu, A., Parsons, A. R., & Trott, C. M. 2014a, *PRD*, 90, 023018
- Liu, A., Parsons, A. R., & Trott, C. M. 2014b, *PRD*, 90, 023019
- Majumdar S., Bharadwaj S., Choudhury T. R., 2013, *MNRAS*, 434, 1978
- Mao, X.-C. 2012, *ApJ*, 744, 29
- McQuinn, M., Zahn, O., Zaldarriaga, M., Hernquist, L., & Furlanetto, S. R. 2006, *ApJ*, 653, 815
- Mellema, G., et al. 2013, *Experimental Astronomy*, 36, 235
- Morales, M. F., & Hewitt, J. 2004, *ApJ*, 615, 7
- Morales, M. F., & Wyithe, J. S. B. 2010, *ARAA*, 48, 127
- Neben A. R. et al., 2016, arXiv:1602.03887
- Nuttall Albert H., 1981, *IEEE Transactions on Acoustics, Speech, and Signal Processing*, ASSP-29, 84
- Paciga G. et al., 2011, *MNRAS*, 413, 1174
- Paciga, G., Albert, J. G., Bandura, K., et al. 2013, *MNRAS*, 433, 639
- Parsons A. R. et al., 2010, *AJ*, 139, 1468
- Parsons, A. R., Pober, J. C., Aguirre, J. E., et al. 2012, *ApJ*, 756, 165
- Parsons, A. R., Liu, A., Aguirre, J. E., et al. 2014, *ApJ*, 788, 106
- Planck Collaboration, P. A. R. Ade et al., Planck 2015 results. XIII. Cosmological parameters, arXiv:1502.01589.
- Pober J. C. et al., 2013, *ApJL*, 768, L36
- Pober, J. C., Parsons, A. R., DeBoer, D. R., et al. 2013a, *AJ*, 145, 65
- Pober, J. C., Liu, A., Dillon, J. S., et al. 2014, *ApJ*, 782, 66
- Pober, J. C., Hazelton, B. J., Beardsley, A. P., et al. 2016, arXiv:1601.06177
- Prasad, P., Subrahmanya, C. R. 2011, *Experimental Astron.*, 31, 1.
- Pritchard, J. R. and Loeb, A., 2012, *Reports on Progress in Physics* 75(8), 086901
- Santos, M.G., Cooray, A. & Knox, L. 2005, 625, 575
- Shaver, P. A., Windhorst, R. A., Madau, P., & de Bruyn, A. G. 1999, *A & A*, 345, 380
- Thyagarajan, N., Udaya Shankar, N., Subrahmanyan, R., et al. 2013, *ApJ*, 776, 6
- Thyagarajan, N., Jacobs, D. C., Bowman, J. D., et al. 2015, *ApJL*, 807, L28
- Tingay, S. et al. 2013, *Publications of the Astronomical Society of Australia*, 30, 7
- Trott, C. M., Wayth, R. B., & Tingay, S. J. 2012, *ApJ*, 757, 101
- Trott, C. M., Pindor, B., Procopio, P., et al. 2016, *ApJ*, 818, 139
- van Haarlem, M. P., Wise, M. W., Gunst, A. W., et al. 2013, *A & A*, 556, A2
- Vedantham, H., Udaya Shankar, N., & Subrahmanyan, R. 2012, *ApJ*, 745, 176
- Yatawatta, S. et al. 2013, *Astronomy & Astrophysics*, 550, 136